MIT Libraries | DSpace@MIT

MIT Open Access Articles

Examining flow-flame interaction and the characteristic stretch rate in vortex-driven combustion dynamics using PIV and numerical simulation

The MIT Faculty has made this article openly available. ***Please share*** how this access benefits you. Your story matters.

Citation: Hong, Seunghyuck, Raymond L. Speth, Santosh J. Shanbhogue, and Ahmed F. Ghoniem. "Examining Flow-Flame Interaction and the Characteristic Stretch Rate in Vortex-Driven Combustion Dynamics Using PIV and Numerical Simulation." Combustion and Flame 160, no. 8 (August 2013): 1381–97.

As Published: http://dx.doi.org/10.1016/j.combustflame.2013.02.016

Publisher: Elsevier

Persistent URL: http://hdl.handle.net/1721.1/98853

Version: Author's final manuscript: final author's manuscript post peer review, without publisher's formatting or copy editing

Terms of use: Creative Commons Attribution

Massachusetts Institute of Technology

Examining flow-flame interaction and the characteristic stretch rate in vortex-driven combustion dynamics using PIV and numerical simulation

Seunghyuck Hong, Raymond L. Speth, Santosh J. Shanbhogue, Ahmed F. Ghoniem*

Reacting Gas Dynamics Laboratory, Center for Energy and Propulsion Research
Department of Mechanical Engineering, Massachusetts Institute of Technology,
77 Massachusetts Avenue, Cambridge, MA 02139, United States

Abstract

In this paper, we experimentally investigate the combustion dynamics in lean premixed flames in a laboratory scale backward-facing step combustor in which flame-vortex driven dynamics are observed. A series of tests was conducted using propane/hydrogen/air mixtures for various mixture compositions at the inlet temperature ranging from 300 K to 500 K and at atmospheric pressure. Pressure measurements and high speed particle image velocimetry (PIV) are used to generate pressure response curves and phase-averaged vorticity and streamlines as well as the instantaneous flame front, respectively, which describe unsteady flame and flow dynamics in each operating regime. This work was motivated in part by our earlier study where we showed that the strained flame consumption speed S_c can be used to collapse the pressure response curves over a wide range of operating conditions. In previous studies, the stretch rate at which S_c was computed was determined by trial and error. In this study, flame stretch is estimated using the instantaneous flame front and velocity field from the PIV measurement. Independently, we also use computed strained flame speed and the experimental data to determine the characteristic values of stretch rate near the mode transition points at which the flame configuration changes. We show that a common value of the characteristic stretch rate exists across all the flame configurations. The consumption

*Corresponding author. 77 Massachusetts Avenue, Room 3-344, Cambridge MA 02139, USA. Fax: +1-617-253-5981. E-mail: ghoniem@mit.edu

speed computed at the characteristic stretch rate captures the impact of different operating parameters on the combustor dynamics. These results suggest that the unsteady interactions between the turbulent flow and the flame dynamics can be encapsulated in the characteristic stretch rate, which governs the critical flame speed at the mode transitions and thereby plays an important role in determining the stability characteristics of the combustor.
Keywords: Stretch rate, Particle image velocimetry, Flame-vortex interaction, Strained flame speed, Consumption speed, Mode transition

---

Nomenclature

Greek

δ_f	Flame thickness
η	Kolmogorov length scale
Γ	Circulation of the vortex
ν	Kinematic viscosity
ω	vorticity
ϕ	Equivalence ratio
ϕ^*	Critical equivalence ratio at which the mode-transitions are observed
ρ_b	Density of burned mixture
ρ_u	Density of unburned mixture
κ	Flame stretch rate
$\overline{\kappa}$	Average stretch rate along the flame surface
$\tilde{\kappa}$	Non-dimensional flame stretch rate parameter, defined in Eq. (5)

$\tilde{\kappa}^*$ Common value of the characteristic stretch rate for the operating conditions at which the mode-transition occurs

Roman

Re Reynolds number

$\mathrm{Re_L}$ Turbulent Reynolds number

c Speed of sound

f An oscillation frequency

H Step height (20 mm)

L_c Characteristic length of geometry

l_G Gibson length scale

p' Pressure fluctuations

u' Flow velocity fluctuations

u'_0 The rms value of the velocity fluctuations in the unburned gas region

U_u Bulk velocity of the unburned mixture

$\tilde{S}$ Non-dimensional flame speed parameter, defined in Eq. (4)

$\tilde{S}^*$ Common value of the characteristic flame speed for the operating conditions at which the mode-transition occurs

S_c Flame consumption speed

s_d Flame displacement speed

$\mathrm{T_{in}}$ Temperature of the inlet mixture

$\mathrm{X_{H_2}}$ Mole fraction of hydrogen in the fuel mixture

1. Introduction

Combustion instability has been one of the most critical phenomena encountered during the development of gas turbine combustors used for propulsion and power generation as well as augmenters, industrial burners and rocket engine. This instability is often observed in lean premixed mode (LPM) of combustion, where high amplitude pressure and flow oscillations, i.e., thermoacoustic instabilities, can cause flame extinction and flashback as well as significant noise and structural damage. Thermoacoustic instabilities are resonant phenomena that result from positive feedback interactions among the combustion process, acoustic modes, and unsteady flow dynamics when the heat release fluctuation is properly phased with the pressure oscillation.

Several mechanisms are known to promote the unsteady coupling processes; e.g., flame-acoustic wave interactions, flame-vortex interactions, equivalence ratio fluctuations, flame-wall interactions and the effect of unsteady stretch rate, which may be present individually or concurrently [1]. Flame-vortex interactions are among the most significant instability mechanisms in large-scale gas turbine combustors [2, 3]. When the unsteady heat release rate fluctuations associated with the large-scale coherent vortical structures couple positively with the acoustic field, self-sustained acoustic oscillations are observed [4, 5, 6, 7, 8, 9, 10].

In this paper, we present an experimental study on the mechanism of the combustion instability driven by flame-vortex interactions. In particular, we focus on the estimation of the flame stretch induced by the interaction between the flame front and the unsteady vortex shed at the sudden expansion, which, as described below in detail, has been left out in our previous study [10], while the stretch rate is an essential parameter for correlating the combustor dynamics.

A number of previous studies on the flame-vortex interaction have emphasized the role of large-scale vortical structures and their kinematics (formation, separation and convection) in the combustion instabilities observed in such configurations. Poinsot et al. [5] examined the low-frequency instabilities in a multi-inlet dump combustor, demonstrating that vortex shedding, convection and acceleration lead to an intense reaction providing short durations

of high heat release, which, with suitable timing relative to the pressure, can drive large amplitude oscillations. Yu et al. [7] demonstrated that the unstable characteristics in a dump combustor are governed by periodic vortex shedding and convection associated with the acoustic velocity fluctuations, which drive large-scale flame front motion. They predicted the instability frequency based on the vortex convection time in the combustor and the acoustic feedback time, i.e., the time taken for a pressure disturbance to travel up the inlet system and back. These studies [5, 7] provide evidences that the unsteady heat release fluctuations associated with the vortical structure satisfy the in-phase relationship with the pressure fluctuations while driving the instability. The chemiluminescence emissions from C_2^* or CH^* radicals indicate that an intense burning occurs when the vortex structure collides with obstacles, e.g., a downstream nozzle exit or the combustor wall, leading to the maximum heat release rate. In this context, Matveev and Culick [8] proposed the models for vortex shedding and burning. In their "kicked" oscillator model, the burning process is assumed to be localized in space and time, occurring only at the moment of the vortex impingement on the wall, where the unsteady heat release rate is expressed using a delta function. This model is, however, rather oversimplified, as the burning (and hence, the heat release rate) is distributed in time and space in reality.

Some of prior studies put efforts into finding an appropriate parameter that correlates the combustion characteristics, e.g., heat release rate, flame dynamics, mode transitions, etc. Ahn and Yu [9] investigated the spacial distribution of local heat release rate fluctuations within the vortex structure. The results showed the correlation between the Damköhler number and the local heat release rate fluctuations, suggesting possible applications of active control strategy using secondary fuel injections. Altay et al. [10] demonstrated that a heat release parameter, which incorporates the strained flame consumption speed[1] and volumetric gas expansion across the flame, can correlate well the combustor dynamics data,

[1]The consumption speed is defined as $S_c = \frac{\int_{-\infty}^{\infty} q'''/c_p dy}{\rho_u(T_b - T_u)}$, where q''' is the volumetric heat release rate, c_p is the specific heat of the mixture, y is the coordinate normal to the flame, and T_u and T_b are the unburned and burned gas temperature, respectively.

e.g., the dynamic pressure measurements and high speed flame images. They used similar observations to those made by Poinsot et al. [5] and Yu et al. [7] that the maximum heat release rate coincided with the moment when the large wake vortex collides with the upper wall of the combustor, to find a correlation between the instability period and the heat release parameter. They demonstrated that the strained flame consumption speed parameter can be used to collapse the pressure response curves−the pressure amplitude as a function of equivalence ratio−obtained over a wide range of operating conditions in a backward-facing step combustor. Similar work was presented by Speth and Ghoniem [11], where they used the consumption speed to collapse the pressure response curves obtained in a swirl-stabilized combustor. These studies [10, 11] used numerical results of a strained flame model to determine the consumption speed under different operating conditions, where the consumption speed depends on the thermochemical properties of the mixture and the flame stretch rate. However, in previous work [10, 11], the value of stretch rate at which the consumption speed was calculated was chosen by trial and error, i.e., by experimenting with different values until a value was found that collapses the experimental data over the range of conditions.

In this paper, we present an analysis that improves the previously mentioned drawbacks of [10, 11] by establishing a more systematic method to determine the characteristic stretch rate at which the flame speed should be calculated. We use the numerical results of strained flame model [12, 13] as well as the experimental results in which we perform the dynamic pressure measurement and the high speed particle image velocimetry (PIV) at various operating conditions in a 50-kW laboratory scale backward-facing step combustor.

Particle image velocimetry has been widely used to study the spatial structure of turbulent flow in non-reacting flow cases (see [14] and the references therein for examples) and in reacting flow cases (after successful applications [15, 16]). The PIV technique, in which the entire flow field can be resolved, is advantageous to studying the interaction bewteen the flame surface and the flow, compared to the point velocity measurements such as laser Doppler velocimetry (LDV) or using a hot wire anemometer. While the conventional PIV measurements were performed at low repetition rate (e.g., 10 Hz), recent development in

high-speed lasers and cameras contributed to the high-repetition-rate measurements (on the order of kHz), which advanced the capabilities for resolving a wide spectrum of time and length scales; e.g., these advanced techniques were applied to swirl-stabilized combustors [17, 18, 19] and to two-dimensional Bunsen slot burners [20, 21, 22, 23]. Some of previous studies reported the measurement of turbulent flame properties in two-dimensional Bunsen flames using such techniques [21, 22, 23, 24]. The application of the high speed PIV measurement to the step-stabilized turbulent reacting flow has been very limited in literature.

In this study, the high-speed PIV measurements are performed to 1) examine the interaction between the flow and flame dynamics and to 2) quantify the stretch rate along the flame front. In previous studies [5, 6, 7, 10], the flame chemiluminescence measurements were used to examine the combustor dynamics, which were limited to the qualitative description of the flame motions. The velocity measurement was performed only at a point using a hot wire (film) anemometer [7, 10]. The PIV measurement allows us to better understand the flow-flame interaction by visualizing the entire flow field as well as its correspondence with the flame front topologies, as discussed in Section 3.2. In Section 4.1, we also directly estimate the stretch rates using the instantaneous flame images and the velocity field obtained from the PIV data. The results for selected cases in each operating regime indicate that the stretch rate used for flame speed calculations in [10] is one order of magnitude higher than the measured values. To determine the appropriate values of the stretch rate for the operating conditions used in the experiment, we present an analysis based on the premise that there are common values of the normalized stretch rate and flame speed at a family of operating conditions at which the flame exhibits a similar configuration as identified by the flame images. This is discussed in Section 4.2. Our analysis shows that common values of the characteristic stretch rate and the corresponding consumption speed indeed exist, which can be used to collapse the pressure response curves over the full range of operating conditions.

The rest of the article is structured as follows. Section 2 describes the combustor configuration and diagnostics including high-speed PIV as well as the experimental conditions. In Section 3, we present the pressure and PIV data to examine the combustor dynamics at

various operating conditions. Section 4 describes our effort to estimate the stretch rate for the flame speed calculations. The article ends with concluding remarks in Section 5.

2. Experimental Apparatus

2.1. Combustor configuration with instrumentations

Figure 1 shows a diagram of the backward-facing step combustor. The combustor consists of a rectangular stainless steel duct with a cross section 40 mm high and 160 mm wide. The air inlet is choked. At a location 0.45 m downstream from the choke plate, a 0.15 m long ramp reduces the channel height from 40 mm to 20 mm, followed by a 0.4 m long constant area section that ends with a sudden expansion back to 40 mm. The step height is 20 mm. The overall length of the combustor is 5 m. A circular exhaust pipe comprises the last 3 m of the combustor with a cross sectional area approximately four times that of the rectangular section. The exhaust exits to a trench with a large cross sectional area. Quartz viewing windows 0.4 m wide is installed in the vicinity of the step, providing optical access.

An Atlas Copco GA 30 FF air compressor supplies air up to 110 g/s at 883 kPa. A pair of Sierra C100M Smart-Trak digital mass flow controllers allows maximum flow rates of 2.36 g/s for propane and 0.30 g/s for hydrogen. The uncertainty of the flow rate is $\pm 1\%$ of the full scale, which allows the equivalence ratios to be measured with the accuracy of $\Delta\phi \sim 0.002$. Fuel is injected through several spanwise holes in a manifold located 0.96 m upstream of the step, which is 0.02 m downstream of the chock plate. Since the fuel is injected near the chock plate where flow velocity oscillations are weak, the amplitude of equivalence ratio oscillations established at the fuel injector is small. This was confirmed by the equivalence ratio measurements, which can be found in our previous study [10].

Air is preheated to a temperature of up to 500 K using an Osram Sylvania 18 kW inline resistive electric heater. The temperature of the inlet mixture is measured using a type K thermocouple mounted 0.2 m upstream of the sudden expansion.

Pressure is measured at three locations: 0.20 m upstream of the sudden expansion and 0.25 m downstream from the beginning of the exhaust pipe using Kulite MIC-093 high intensity microphones mounted in semi-infinite line configurations [25], and 0.15 m downstream

of the choke plate using a flush-mounted, water-cooled Kistler 7061B pressure sensor. The pressure sensors were sampled at 10 kHz, synchronized with the high-speed camera for PIV measurement.

All data are acquired using a National Instruments PCIe-6259 data acquisition board and the Matlab Data Acquisition Toolbox. A custom Matlab code is used to store the data and control the experiment.

2.2. High-speed particle image velocimetry

Planar velocity fields and flame surface topology were obtained using phase-locked particle image velocimetry (PIV). The schematic of setup is shown in Fig. 2. The light source consists of a Nd:YLF laser of wavelength 527 nm capable of producing dual pulses at a rate up to 5 kHz with a peak power output of 25 mJ/pulse. A 1280 $\times$ 1024 pixel NAC GX-1 CMOS camera, with an F-mount Nikon 60 mm micro-lens with an aperture of $f/8$ was used for imaging. The interval between the laser pulses was set to $10-30$ μs depending on the flow velocity. A light sheet less than 1 mm thick in the imaged region was generated using a spherical lens with a focal length of 1000 mm and a cylindrical lens with a focal length of -20 mm. The former was used to reduce the diameter of the beam and the latter was used to diverge the beam to generate a sheet. Bypass air, taken from the inlet pipe upstream of the choke plate, is routed through a cyclone-type seeder. Seeding particles consisting of $1.5-3$ μm diameter Al_2O_3 are injected into the main air immediately downstream of the choke plate. The PIV measurements are processed using the LaVision DaVis 7.2 software.

The distance between the imaging plane and the camera was set to $\sim$0.6 m based on the desired field of view. The corresponding viewing area for the PIV measurements is 120 mm $\times$ 120 mm, generating 800 $\times$ 800 pixel images of the seeding particles. These images are processed using a multi-pass approach, with the final pass using a 16 $\times$ 16 pixel window with 50 % overlap. This produces velocity fields with a spatial resolution of 1.14 mm. The properties of PIV measurements are summarized in Table 1, and the PIV data are discussed in Sections 3.2 and 4.1.

Table 1: Properties of high-speed PIV measurement

Property	Specification
Frame rate (Hz)	1000
Temporal resolution (ms)	1
Field of view (mm^2)	120×120
Camera resolution ($pixel^2$)	800×800
One pixel size (mm/pixel)	0.143
Interrogation box (mm)	2.29
Overlap	50 %
Spatial resolution (mm)	1.14

2.3. Experimental conditions

To investigate the stability characteristics of the combustor, we conducted a series of experiments where the inlet conditions were varied while dynamic pressure was recorded. We varied the fuel composition in C_3H_8:H_2 volume ratios corresponding to 50:50, 70:30, and 100:0, and varied the inlet temperature from 300 K to 500 K in increments of 100 K. For each fuel composition and inlet temperature, we varied the equivalence ratio of the fuel-air mixture from near stoichiometry toward the lean blow-off limit. At the inlet temperature of 300 K, we obtain the particle image velocimetry measurements in each operating regime.

Throughout all tests, the combustor was operated at atmospheric pressure and at the constant Reynolds number of 6500 based on the step height of 20 mm. This corresponds to a mean inlet velocity of 5.2 m/s at 300 K, which increases to 8.5 m/s at 400 K, and 12.5 m/s at 500 K. The inlet velocity varies by less than $\sim 10\%$ as a function of fuel composition and equivalence ratio.

3. Combustor Dynamics

3.1. Pressure response

The combustor exhibits distinct dynamic regimes depending on the operating parameters. In each operating regime, we observe different pressure response as well as distinct flame dynamics. Altay et al. [10] performed a parametric study in the same combustor to define its stability map. Pressure amplitudes and frequencies were presented as a function of the

equivalence ratio for propane/hydrogen/air mixtures at different Reynolds numbers, inlet temperatures and fuel compositions. Similar work was performed using syngas/air mixtures in a step combustor [26, 27] and in a swirl-stabilized combustor [11, 28].

In this section, we describe the key characteristics of the pressure response under different conditions. In particular, we highlight the impact of fuel composition and inlet temperature on the operating regime. The correspondence between the pressure response and the PIV results will be discussed in Section 3.2, which reveal the interactions between the flame front and unsteady flow field in each operating regime. In Section 4, the PIV data are used to determine the characteristic stretch rate.

3.1.1. Baseline case

Figure 3 shows the overall sound pressure level (OASPL) as a function of equivalence ratio for a propane/air mixture at T_{in} = 300 K. The OASPL in dB is defined as:

$$\mathrm{OASPL} = 10 \log_{10} \overline{\left[\frac{p(t) - \overline{p(t)}}{p_0} \right]^2} \tag{1}$$

where overbars indicate average values, $p(t)$ is the pressure measured in an interval $t_1 < t < t_2$ and $p_0 = 2 \times 10^{-5}$ Pa. The pressure signal measured at 0.2 m upstream of the sudden expansion (where the flame is nominally anchored) is used for calculating the OASPL. The peak frequency at which the pressure oscillation is at its maximum is represented by colors of the markers.

The pressure response curve shows three distinct bands depending on the equivalence ratio, as seen in Fig. 3. Near the lean blow-off limit, the oscillation amplitude is below 140 dB and, as will be seen in the PIV data in Section 3.2, the flame exhibits a relatively stable motion. We refer to this band as *Mode I*. As the equivalence ratio is gradually increased, the amplitude grows to $\sim$ 140−145 dB, which is referred to as *Mode II*. In this regime, we observe a weak oscillation at 40 Hz. At higher equivalence ratios, the OASPL jumps to 150−160 dB, and we refer to this band as *Mode III*. In Mode III, the combustor exhibits strong oscillations at two different frequencies: $\sim$40 Hz at relatively low equivalence ratios

and ∼70 Hz at higher values. In the rest of the paper, we distinguish these two unstable regimes by referring to the regions where the combustor exhibits oscillations at ∼40 Hz and ∼70 Hz as *Mode IIIa* and *Mode IIIb*, respectively. The transition between different operating regimes occurs as the equivalence ratio exceeds a certain threshold.

3.1.2. Impact of fuel composition and inlet temperature

In Fig. 4, we plot the pressure response curves for different fuel composition and inlet temperature; for pure propane and propane/hydrogen (50% each by volume) fuel mixture at the inlet temperatures of 300 K and 500 K. For a fixed inlet temperature, as the hydrogen concentration in fuel mixtures increases, the pressure response curve shifts to the left while exhibiting the same operating regimes, indicating that the mode transitions occur at lower equivalence ratio. The same impact is observed as the inlet flow is preheated to higher temperature. The pressure responses at T_{in} = 500 K are similar to those at T_{in} = 300 K, except that the response curves shift to the left, i.e., the mode transitions occur at leaner conditions. In addition, the range of equivalence ratio corresponding to Mode II is narrower than that at T_{in} = 300 K.

The change in the mixture composition does not significantly impact the instability frequencies. However, as the inlet temperature is raised to 500 K, we observe two changes in the frequencies. First, the range of equivalence ratio corresponding to Mode IIIb (unstable at 70−90 Hz) is much larger than that at T_{in} = 300 K. Second, the frequency of oscillation in Mode IIIb increases as the inlet temperature is raised, e.g., from ∼70 Hz at T_{in} = 300 K to ∼90 Hz at T_{in} = 500 K, whereas the frequencies in Mode IIIa remain constant at ∼40 Hz. In a parallel study [29], we present an acoustic analysis that shows the correspondence between each unstable regime and the longitudinal acoustic mode of the combustor, e.g., the quarter-wave (fundamental) or the three quarter-wave (first harmonic) acoustic modes.[2] The one-dimensional acoustics model suggests that Mode IIIb (70−90 Hz) corresponds to

[2]The acoustic analysis is not shown here since it is of no particular importance within the scope of this study, where we examine the flow and flame dynamics using the PIV data and correlate the dynamic instabilities with the flame speed and stretch rate, as will be discussed in the subsequent sections.

the three quarter-wave acoustic mode while Mode IIIa (40 Hz) resembles the quarter-wave acoustic mode. Since the natural frequency, f, is proportional to the speed of sound, c, which increases as the square root of the gas temperature, T ($f \sim c \sim \sqrt{T}$), the increase in the natural frequency at higher inlet temperature is expected. A detailed acoustic analysis as well as the mode shape of each pressure oscillation can be found in Ref. [29].

3.2. Particle Image Velocimetry

Distinct flame dynamics can be observed in each operating regime using the flame chemiluminescence images [10, 29]. In order to examine the flame-flow interactions that give rise the combustion dynamics, it is necessary to study the correspondence between the flow field and the flame front motion. In this section, we examine the flame and flow dynamics using the particle image velocimetry (PIV) data in each operating regime.

3.2.1. Post-processing the PIV data

High-speed flame chemiluminescence images presented in [10] show the periodic large-scale flame dynamics associated with the vortical structure. Several earlier studies [4, 5, 6, 7] also demonstrated that large-scale coherent vortical structures play an important role in dynamic instabilities observed in a dump combustor configuration. To identify the large-scale characteristics of the periodic flow field as well as the flame front motion, the instantaneous PIV data obtained in Mode II and Mode III, where the combustor exhibits periodic oscillations, are phase-averaged. Phase-averaging allows one to capture the coherent flow patterns by filtering out the incoherent, random fluctuations [30, 31, 32]. For the steady flame observed in Mode I, where the phase of periodic motion is not defined, the time-average image as well as the instantaneous images are examined.

To obtain the phase-averaged data, we use simultaneous measurements of the dynamic pressure and the PIV. The pressure signal is used as the reference for calculating the phase during the instability cycle. A best-fit sine function for the pressure signal is calculated for a time interval spanning two periods of the cycle, from which the phase corresponding to the velocity field is computed. The phase-range from 0 to 2π is divided evenly into a

number of intervals (e.g., total 60 intervals encompassing the entire cycle, each of which corresponds to 6°). The instantaneous PIV data recorded over ∼120 instability cycles are then grouped by the corresponding phase (interval) of the synchronized pressure signal, and an ensemble average in each interval is taken. The phase-averaged velocity and vorticity fields are generated with a spatial resolution of ∼1 mm using the instantaneous data obtained from LaVision Davis 7.2 software package (see Section 2.2 for the PIV properties).

Figure 5 shows sample images of the PIV results. The raw seeding particle image is shown in Fig. 5(a). A sample of the phase-averaged vorticity field and the streamlines are shown in Fig. 5(b),[3] where the flow direction is indicated by arrows and the magnitude of the vorticity is depicted by colors, blue indicating counter clockwise vorticity and red indicating clockwise vorticity. The vorticity is calculated from the velocity vectors in adjacent grid points using a second-order central difference scheme.

To examine the flame-flow interactions, we also need to define the flame front location. A number of previous studies performed CH- or OH-planar laser-induced fluorescence (PLIF) measurements to define the flame front location, in which the gradients of CH or OH radical signal were used to indicate the flame front position [18, 19, 24, 33]. The flame front can also be detected from the abrupt change in the seeding particle densities between the reactants and the products [34, 35] (see Fig. 5a). For turbulent premixed flames, this method can be used to determine the flame front location when premixed combustion is in the thin reaction zones regime or the flamelet regime [36]. In these regimes, which are common to the practical applications of premixed turbulent combustion, the flow field can be considered as composed of two regions: unburned and burned regions, separated by a thin interface, i.e., the flame front where the chemical reactions take place. The flame front can locally be considered as a thin laminar flame, although its inner structure and the flame speed can slightly differ from those of the laminar flame due to the impact of wrinkling and stretch [37]. Pfadler et al. [38] performed simultaneous OH-PLIF and PIV measurements in a V-shaped flame,

[3]Plotting the vorticity field and the velocity vector field together with the flame brush (as shown in Figs. 6, 9 and 12) makes the figure too complex. Hence, the streamlines are plotted instead of the velocity vector field to enhance legibility.

demonstrating that the flame front locations detected from the PIV seeding image and OH radical concentration show good agreement within the accuracy of ~ 0.1 mm.

In this study, we use the raw seeding image of the PIV measurement to detect the instantaneous flame front position as depicted in Fig. 5(c). The flame front position is determined based on the local maxima of the density gradients in the seeding image using the Canny edge detection method [39]. The spatial resolution of the flame front line is $\sim$ 0.14 mm. The flame thickness at the pressure and temperature at which the experiments are conducted in this study is estimated to be ~ 1 mm [12], and thus, the PIV measurements herein provide a sufficient accuracy for detecting the flame front location.

The flame front lines are used along with the phase-averaged vorticity fields and streamlines to qualitatively examine the flame and flow dynamics in the following section. In Section 4.1, the instantaneous flame lines are used to quantify the flame stretch. For Mode II and Mode III, the instantaneous flame front lines are grouped by the phase identified using the synchronized pressure measurement, and the ensemble of the instantaneous flame lines at a given phase are overlapped to generate the flame brush as depicted in Fig. 5(d). For the steady flame (Mode I), we generate the flame "brush" by overlapping the instantaneous flame lines corresponding to the velocity and vorticity fields that are used to generate the time-average data.

3.2.2. Flame and flow dynamics

Here, we generate combined images of the vorticity field, streamlines and flame brush, samples of which are shown in Fig. 5b and Fig.5d. The vorticity field and the streamlines describe the unsteady flow, e.g., the formation and evolution of the vortical structure, while the flame brush illustrates unsteady flame motion.

For Mode IIIa and Mode II, the combined images at six different phases comprising the cycle are shown in Figs. 6 and 9, respectively. At the bottom of these figures, the pressure and flow velocity measured upstream of the sudden expansion as well as the flow acceleration are plotted against the phase of the cycle. We also quantify the properties of the large vortex as a function of the phase during the entire cycle in Figs. 8 and 10, in which we show the x-

and y-position of the vortex core (the center of the vortex), i.e., the horizontal and vertical distance from the edge of the step (see Fig. 7), as well as the total vorticity integrated over the vortex structure, i.e., the circulation (Γ) of the vortex, defined as $\Gamma = \left|\int_A \omega \, dA\right|$ where ω is the vorticity and A is the area in which the vortex structure exists. The circulation of the vortex, therefore, essentially reflects the size of the vortex as well as the magnitude of the vorticity. As will be shown later in this section, the circulation turns out to be a good surrogate for evaluating the periodic evolution of the vortex structure during the cycle. For Mode I, the instantaneous images are shown in Fig. 11. The time-average values of ∼1000 images are also presented in Fig. 12.

Mode III. Figure 6 shows the post-processed PIV data covering one instability cycle measured at $\phi = 0.75$ at $T_{in} = 300$ K for propane/air mixture. Throughout the instability cycle, the vortex formed downstream the edge of the step drives the evolution of the flame brush. The combustor exhibits significant pressure and flow oscillations at 40 Hz, where the pressure leads the flow velocity by 90°. The flow fluctuations are significant, where the magnitude is about twice the mean value. A flow reversal is observed during the cycle, for the time spanning $\sim 20 - 30\%$ of the instability period, which induces the observed flame flashback. Similar flame motions can be observed in the flame chemiluminescence images [10], whereas the details of the flow field, e.g., size, position and circulation of the vortex as well as a flow reversal during the flame flashback, are revealed here by the PIV measurements. We describe below the combustor dynamics observed in Mode IIIa (Figs. 6 and 8) during one instability cycle.

In Fig. 6, we observe that a small vortex with large vorticity is formed at the sudden expansion when the flow acceleration is at its maximum (between b and c). As the flow velocity exceeds its mean value, approaching a maximum (c-d), the vortex grows and convects downstream, and the flame wraps itself around the vortex edge (c-e). Figure 8 shows that the vortex core position moves downstream nearly at a constant speed, approaching the bottom wall of the combustor (b-c-d), while at the same moment, the total vorticity within the vortex structure gradually increases. When the flow velocity reaches its maximum and

thereafter starts to decrease (d-e), the vortex is nearly stationary (see Fig. 8d-e), and the flame brush shows approximately flat lines near the step as seen in Fig. 6(d-e). Meanwhile, as seen in Fig. 8, the vortex exhibits the largest circulation (close to e), which lags the flow oscillations by ∼60°.

When the flow velocity drops below its mean value (f), the circulation of the vortex becomes smaller but still growing in size. In the meantime (between e and f), the vortex accelerates its convection toward downstream (see Fig. 8e-f). While the flow velocity is below its mean value (f-a-b), the flame moves toward the upper wall along with the vortex structure (see Fig. 6f-a and Fig. 8f-a), starting to propagate upstream of the step toward the inlet section. The circulation of the vortex becomes even smaller (f-a-b), which gradually convects downstream with its center location exhibiting an oscillatory movement, i.e., moving back and forth in the horizontal direction (see Fig. 8f-a-b). The negative flow velocity near its minimum (a) induces the flow reversal, accelerating the flame flashback. In the meantime, the vortex structure collides with the upper wall (f-a), and its size is limited by the combustor channel height. The flame chemiluminescence images recorded in the same configuration [10] showed that the collision between the flame and the upper wall induces an intense burning of the reactant packet behind the flame, leading to an increase in heat release rate.

As the flow velocity departs from its minimum and becomes positive values (a-b-c), the flame moves back downstream. The flame is anchored at the step (c), wrapping itself around the edge of the new vortex shed in the next cycle. Combustion dynamics in Mode IIIb, although not shown here, are similar to those in Mode IIIa, except that the flame is more compact and propagates further upstream when it flashes back.

Mode II. Figure 9 shows combustion dynamics in Mode II. The PIV data were obtained at $\phi = 0.58$ at $T_{in} = 300$ K burning propane/hydrogen (50% each by volume) fuel mixture. Similarly, the combustor oscillates at 40 Hz, where the pressure leads the flow velocity by 90°. However, the oscillation amplitudes are much weaker than those in Mode III; e.g., the maximum pressure oscillation is ∼500 Pa, and the flow fluctuations are about half of the mean value. The vorticity field also shows weaker magnitude, where the maximum value is

approximately half of that in Mode III. The flow reversal is not observed, and the mean flow moves in the forward direction during the entire cycle. As a result, the flame brush does not exhibit flashback, but shows flapping motion around the vortex edge while remaining attached to the step.

Similarly, a vortex is formed at the step near the maximum flow acceleration (between b and c in Fig. 9). The vortex grows and convects downstream while the flame wraps itself around the vortex edge (c-d-e-f). On the contrary to Mode III, Fig. 10 shows that the vortex convects downstream nearly at a constant speed during the entire cycle. The vertical location of the vortex core is nearly constant, while gradually approaching the bottom wall of the combustor as it diminishes downstream near the end of the cycle. The overall circulation of the vortex (see Fig. 10) is smaller than that observed in Mode III, and its size is also smaller (see Fig. 9). For example, in Fig. 9(f), the height of the vortex is similar to the step height and its structure is not as contiguous to the expansion plane as in Mode IIIa, i.e., its center is located further downstream (compare Fig. 10d-f with Fig. 8d-f), whereas in Fig. 6(f), the growth of vortex structure seems to be limited by the combustor channel height, and its upstream edge touches the sudden expansion plane.

Figures 9 and 10 show that as the flow velocity drops below the mean value (Fig. 9e-f), the vortex exhibits the largest circulation (Fig. 10e-f), lagging the velocity oscillations by $\sim$90°. In the meantime, the flame brush starts to rise toward the upper wall (e-f), sitting on the top edge of the vortex (f-a-b). As the flow is again accelerated (a-b), Fig. 10 shows that the vortex structure convects downstream toward the combustor exit with a decreasing vorticity, and the small secondary recirculation zone forms between the convecting vortex and the sudden expansion plane (Fig. 9a-b). As the flow velocity increases above the mean value (c), the flame starts to roll up the new vortex formed at the step, which marks the beginning of the next cycle.

Mode I. In Mode I, the phase of periodic motion is not defined and we examine the instantaneous images for the same time period as the instability cycle (e.g., 40 Hz = 0.025 s). Figure 11 shows the PIV data obtained at $\phi = 0.62$ at $T_{in} = 300$ K burning the fuel mixture of

propane and hydrogen (70% and 30% each by volume), where the vorticity field is shown in colored region and the flame front position is indicated by the black line. Streamlines are not shown here for better legibility. Unlike in Figs. 6 and 9, each image in Fig. 11 shows only a single flame front line, as each represents the data recorded at an instant. The pressure and the flow are nearly steady, where their maximum fluctuation amplitudes are very small compared to those in Mode II or Mode III; e.g., $p' < 100$ Pa and $u' < 1$ m/s.

Overall, the instantaneous images clearly show the random nature of turbulent flow field, e.g., the evolution of small vortices and their interaction with the flame front. Small vortices are present in the entire flow field. The vortices with relatively strong vorticity are shed at the sudden expansion. In some cases, e.g., between (b) and (c) as well as (d)−(f), vortex pairing can be observed, leading to a larger structure. The flame surface in the downstream region exhibits a random flapping motion, whereas the flame front near the step remains attached to the step, stabilized by the vortices shed at the step.

Several discontinuities of the flame lines observed in Fig. 11 are due to their inevitable sensitiveness to the threshold values of the particle density gradients used to determine the flame edge from the PIV seeding images. The absence of a line or a break in the flame line should not be taken to indicate local flame extinction, since the flame chemiluminescence measurements in the same flame configuration [10, 29] indicate that there is no clear evidence of local extinction along the flame.

Next, in Fig. 12, we show the time-average vorticity field and streamlines of ∼1000 instantaneous images (recorded for ∼1 second) and the flame brush (overlapped instantaneous flame lines), which are obtained at the same conditions. The flame is anchored at the step, stabilized in the reacting shear layer. In the mean profile, randomly-distributed small vortices are filtered out, whereas large-scale flow structures are depicted. Two recirculation zones are observed; one rotating in clockwise direction between the shear layer and the bottom wall, and another rotating in counter clockwise direction immediately downstream the step. The former is the primary recirculation zone that contributes to the stabilization of a steady flame, whereas the latter is a secondary zone that lies between the primary zone

and the expansion plane, in which the flow circulates in a reverse direction with a relatively weaker vorticity magnitude.

3.3. Summary

The results shown in Figs. 6 and 8−12 demonstrate that a large vortex formed at the edge of the step and its interaction with the flame are important components of the instability mechanism. The kinematics of a growing large vortex shows that the unstable operation of the combustor (Mode III) is associated with the periodic vortex motions featured by sudden acceleration toward downstream and rise toward the upper wall of the combustor, where its size is larger and the circulation, i.e., total vorticity integrated over the vortex structure, is greater than those in Mode II. In Mode III, the strong flow oscillations induce a flow reversal, leading to the flame propagation upstream (flashback) during the part of the cycle.

A comparison of the vorticity field between the different operating regimes indicates that the velocity gradients change as the combustor transitions from one regime to another. This suggests an important role of the strain rate or flame stretch in the transitions between different regimes, as will be discussed in the following section.

While the PIV data describe distinct combustion and flow dynamics in each operating regime, the pressure response curves define the stability map for various inlet conditions. Figure 13 plots the pressure response curves for a range of inlet temperatures and mixture compositions, showing similarities in the combustor response across different inlet conditions. For a fixed inlet temperature and fuel composition, a higher equivalence ratio (ϕ) promotes an unstable operation. We note that a higher equivalence ratio, all else being constant, leads to a higher flame speed. At higher inlet temperature (T_{in}) or higher hydrogen concentration in fuel mixtures (X_{H_2}), the combustor becomes more unstable at lower ϕ, which suggests the important role of the burning velocity in promoting the instability. This motivates our effort to find a combustion parameter that encapsulates the impact of these three parameters (T_{in}, X_{H_2} and ϕ) on the stability characteristics. The laminar burning velocity is perhaps the obvious candidate for the correlating parameter. However, attempts to collapse the data using the laminar burning velocity did not produce satisfactory results [10, 11].

In the next section, we discuss the correlation between a combustion parameter and the experimental data, which, as will be shown, involves determining the flame stretch.

4. Correlation of the Dynamics with Flame Speed and Stretch Rate

Altay et al. [10] demonstrated that the heat release parameter $S_c(\rho_u/\rho_b - 1)$ correlates the combustion dynamics data well, where S_c is the consumption speed of strained flame, ρ_u and ρ_b are the densities of the unburned gas and burned gas, respectively. Similar work was performed by Speth and Ghoniem [11], where they used S_c to collapse the pressure response curves obtained in a swirl-stabilized combustor. As mentioned earlier, the consumption speed S_c is a function of the thermochemical properties of the mixture and the flame stretch rate. Thus, for a given operating condition, the consumption speed depends only on the stretch rate. However, in previous work [10, 11], the values of stretch rate at which the consumption speed was calculated were chosen by trial and error, i.e., such that the pressure response curves for different conditions collapse onto a single characteristic curve. The values of the stretch rate used for correlating the data are $2000-3000$ s^{-1} for the step combustor [10] and 220 s^{-1} for the swirl-stabilized combustor [11].

In this section, we present a more systematic approach to determine the values of the stretch rate at which the strained flame speed should be computed. First, we directly estimate the stretch rate using the PIV data for selected cases as presented in Section 4.1. In Section 4.2, we use the experimental data and the computed strained flame consumption speed to determine the characteristic value of stretch rate for the full range of operating conditions. Finally in Section 4.3, we use the characteristic values found in Section 4.2 to collapse the pressure response curves shown in Fig. 13.

4.1. Stretch rate measurement using the PIV data

A-priori determination of the flame stretch in general requires a detailed map of the velocity field and flame front location. We take advantage of the two-dimensional nature of the flow in the combustor to identify the flame front from the PIV seeding images, as

described in Section 3.2.1 (see Fig. 5c). The stretch of a flame surface element dA is defined in tensor notation [40]:

$$\kappa = \frac{1}{A}\frac{dA}{dt} = (\delta_{ij} - n_i n_j)\frac{\partial u_i}{\partial x_j} + s_d \frac{\partial n_i}{\partial x_i} \tag{2}$$

where δ_{ij} is the Kronecker delta, i and j are indices for each direction in the Cartesian coordinate system (x_i, x_j). The unit vector n is normal to the flame surface toward the unburned gas. The unburned gas velocity and the flame displacement speed are denoted by u and s_d, respectively. The first term in the right hand side is the strain rate induced by the velocity field, while the second term represents the curvature contribution to the flame stretch. Hence, to estimate the stretch rate along the given flame surface, one needs to determine the normal vector to the flame surface, velocity field near the flame, flame displacement speed and the curvature of the flame surface.

The stretch rate is measured for selected cases representing the typical operating regimes discussed in Section 3. The objective of this section is not to generate a detailed map of the flame stretch over a range of conditions (ϕ, T_{in}, X_{H_2}), but compare the experimental value with the one used for the flame speed calculations by Altay et al. [10] in each operating regime. In what follows, we define the conditions of the PIV measurement for which the stretch rate is estimated.

4.1.1. Length scale

Since the underlying flow is turbulent, the flame-flow interactions, which essentially induce the flame stretch, occur at various length scales. For example, the flame can be stretched by the large-scale vortex structure, or can interact with smaller eddies present in the turbulent flow field. The size of flow structure that can be resolved is determined by the spatial resolution of the PIV measurement. Therefore, we need to define the length scale to use in the PIV experiment for estimating the stretch rate.

The PIV results shown in Figs. 6 and 8−12 are obtained with the spatial resolution of ∼0.1 mm and 1.1 mm for the flame line and the velocity field, respectively. For the experimental conditions used in this study, the Kolmogorov length scale $\eta \sim L/\mathrm{Re}_L^{3/4}$ [41]

is estimated to be ∼0.02 mm, where Re_L is the turbulent Reynolds number defined as $u_0'L/\nu$. u_0' is the rms value of the velocity fluctuation in the unburned gas region defined as $u_0' = \overline{(u'^2)}^{1/2} \sim 6$ m/s, ν is the kinematic viscosity of the unburned gas and the largest scale L is taken to be on the order of the step height of 20 mm. It is known that the eddies at the Kolmogorov scale are too weak to stretch the flame effectively, but rather are dissipated due to viscous forces [42, 43]. The size of eddies that can locally interact with the flame front is often referred to as the Gibson scale [44], which is defined as $l_G = s_L^3/\varepsilon$ where s_L is the laminar burning velocity and ε is the average dissipation rate of turbulent kinetic energy. The Gibson length scale is, however, smaller than the Kolmogorov length scale in the thin reaction zones regime ($l_G < \eta < \delta_f$, where δ_f is the flame thickness) [36, 45] and has no physical significance in the present case. In order for turbulent flows to perturb the flame front, the size of eddies should be comparable to the flame thickness δ_f [24, 37], which is estimated here to be ∼1 mm at the pressure and temperature at which the experiments are conducted [12]. Therefore, the spatial resolution of the PIV data shown in Figs. 6 and 8−12 is adequate for resolving the length scale at which the flow structures effectively stretch the flame.

4.1.2. Measurement location along the flame

In addition to the desired spatial resolution, we also need to define the location along the flame where the stretch rate is measured. As previously shown in Figs. 6, 9 and 12, the flame shape and position dynamically change within an operating regime, where in the extreme case (e.g., Mode III, see Fig. 6), the flame propagates upstream during the part of the cycle.

Our primary interest is the region where the flow significantly impact the flame front. Figures 6, 9 and 12 show that the vorticity is at its maximum near the step where the vortex is formed as a result of sudden expansion. Therefore, we anticipate that the flame stretch is at its maximum near the step. Furthermore, Fig. 6 shows that the unstable operation (in Mode III) features the flame detachment from the step and propagation upstream (flashback). Therefore, we speculate that the flame surface elements in the vicinity of the step are more

relevant to the stability characteristics than those downstream. Hence, the stretch rate is quantified along the flame surface near the step. The measurement region in which the stretch rate is estimated is indicated by the red box shown in Fig. 14.

In Mode II and Mode III, we select the phase of the cycle at which the stretch rate is estimated, as the flame front is located in the measurement region during only the part of the cycle. For example, the flame positions at the phases corresponding to Fig. 6(d-e) are taken for the stretch rate measurement. We note that the flow velocity is close to its maximum at these phases, and the flame front lines are nearly flat in the vicinity of the step.

4.1.3. Stretch rate calculation

The flame front lines shown in Fig. 6(d-e), Fig. 9(d-e) and Fig. 12 indicate that the flame surface in the measurement location (red box of Fig. 14) is nearly flat for all the operating regimes. Thus, the curvature term in Eq. (2) can be neglected. The flame stretch then can be rewritten as:

$$\kappa_s = (\delta_{ij} - n_i n_j)\frac{\partial u_i}{\partial x_j} = -n_x n_y \left(\frac{\partial u}{\partial y} + \frac{\partial v}{\partial x}\right) - n_x^2 \frac{\partial u}{\partial x} - n_y^2 \frac{\partial v}{\partial y} \tag{3}$$

where u and v denote the unburned gas velocity in x- and y-direction, respectively. All other variables denote the same as in Eq. (2). The normal vector and the velocity gradient can be computed at each point along the instantaneous flame line. The stretch rate computed using Eq. (3) are then averaged to yield an average stretch rate over the flame surface in the red box (Fig. 14) for a given instant. In each operating regime, such spatially-averaged stretch rates are obtained for approximately $40-50$ instantaneous flame lines. These ensembles of instantaneous spatially-averaged stretch rates are then averaged to compute the final value in each operating regime.

In Table 2, we show the values of the stretch rates computed for selected cases representing different operating regimes. Overall, the stretch rate experienced by the flame front is the largest in Mode III, which decreases in Mode II, being the smallest in Mode I. This result indicates that stronger flow fluctuations in Mode III induce larger stretch on the flame front,

Table 2: Stretch rates computed for the selected operating conditions using C_3H_8/H_2/air mixture at T_{in} = 300 K and Re = 6500.

Operating regime	ϕ	X_{H_2}	$\overline{\kappa}$ (s^{-1})	$\kappa_{min} - \kappa_{max}$ (s^{-1})
Mode III	0.75	0%	301.2	168−430
Mode III	0.73	30%	318.4	164−470
Mode III	0.70	50%	299.4	165−435
Mode II	0.58	50%	255.6	130−381
Mode I	0.62	30%	234.6	129−340

which can be expected by the magnitude of the vorticity field shown in Figs. 6 and 8−12. The first three cases in Table 2, representing different fuel compositions but all corresponding to Mode III, show that the mixture composition does not strongly impact the stretch rate experienced by the flame.

The measured values of the stretch rate shown in Table 2 are one order of magnitude lower than those (e.g., 2000 s^{-1} at T_{in} = 300 K) used for the flame speed calculations in [10]. We again note that the values of the stretch rate used in [10] were determined by trial and error, i.e., by experimenting with different values of the stretch rate until a value was found that collapses the pressure response data onto a single curve, thereby having no physical significance. Moreover, the authors in [10] used the same value of stretch rate for all the operating conditions (ϕ, X_{H_2}) at a given inlet temperature. Since the flame is more stretched in Mode III, larger values of the stretch rate should be used for the flame speed calculations at higher equivalence ratios where the combustor becomes unstable. In the next section, we determine the stretch rate for all the operating conditions used in the experiment, at which the consumption speed should be calculated.

4.2. Determining the stretch rate using experimental and numerical results

In what follows, the consumption speed is calculated using the strained flame model [12, 13], in which a laminar flame is stabilized in a planar stagnation flow, based on the premise that this flame configuration represents the local interaction between the flame and the surrounding flow field presented in Section 3.2. In the strained flame model, reactants are supplied on one side while products are supplied on the other, and the flame stabilizes

in the vicinity of the stagnation point. The products supplied in the counter flow are the equilibrium products at the adiabatic flame temperature corresponding to the supplied reactants mixture. The resultant potential flow velocity field is characterized by the time-varying strain rate parameter. The one-dimensional governing equations for the flame structures are found by using a boundary layer approximation across the flame thickness. The governing equations are discretized using an implicit finite difference method, where the solution is obtained using a preconditioned inexact Newton-Krylov method. Cantera [46] is used to evaluate chemical source terms and the various physical properties. Because of its strong influence on the diffusion of hydrogen, the Soret contribution to diffusive fluxes is included. A reduced chemical kinetic mechanism for propane combustion developed at the UCSD Center of Energy Research [47] is used. More details of the strained flame model and the numerical method can be found in Refs. [12, 13].

4.2.1. Hypothesis

Figure 13 shows similarities in the pressure response as a function of equivalence ratio (ϕ) for various inlet temperatures (T_{in}) and hydrogen concentrations in the fuel mixture (X_{H_2}). It was shown in previous work [10, 11] that the transitions among different regimes can be collapsed using the flame consumption speed, i.e., the combustor transitions from one operating regime to another if the consumption speed exceeds a certain threshold value.

Although not shown here, the flame dynamics, i.e., dynamic changes of the flame shape, also show similarities across different operating conditions (T_{in}, X_{H_2} and ϕ) if the combustor operates in the same regime. Since the flame stretch is a measure of the flame surface variations, we hypothesize here that different flames (burning different mixtures) experience the same "characteristic" stretch rate if they exhibit the same configuration, i.e., the same flame shape or dynamics. Recalling that the consumption speed depends on the stretch rate as well as on the mixture properties, the above hypothesis can lead to the following example: if two flames fired at different conditions are both in Mode III, then the two flames have the same characteristic stretch rate, which induces the consumption speed beyond the critical value for the transition to Mode III.

Now, consider the two unstable flames (in Mode III) established at different inlet temperatures. Given the same Reynolds number (Re = 6500), the flow velocity is larger at higher inlet temperature. Naturally, the flame stretch, which is impacted by the velocity gradient near the flame front, can be larger due to the greater flow velocity at higher inlet temperature. Nonetheless, the "characteristic" stretch rate should be the same to exhibit the same flame configuration. Therefore, the characteristic stretch rate in our hypothesis should be defined such as to encapsulate the impact of different operating conditions while generating a constant value for the same operating regime.

If we consider two flames near the transition point, e.g., both transitioning from Mode II to Mode III, the two flames then not only experience the same characteristic stretch, but also have the same flame speed near the critical value at the transition point. Thus, at the transition point, we expect that different flames share both the characteristic stretch rate and flame speed, which correspond to that flame configuration. Since the flame speed varies depending on T_{in}, X_{H_2} or ϕ, we also need to define the "characteristic" flame speed such that the mixtures at different conditions share the same value at the transition point.

4.2.2. Characteristic stretch rate and flame speed

Here, we define non-dimensional parameters for the flame speed and stretch rate as follow:

$$\tilde{S} = \left(\frac{\rho_b}{\rho_u}\right)\frac{S_c}{U_u} \tag{4}$$

$$\tilde{\kappa} = \left(\frac{\rho_b}{\rho_u}\right)\frac{\bar{\kappa}L_c}{U_u} \tag{5}$$

where the flame speed and the stretch rate are normalized using the bulk velocity of the unburned mixture, U_u, and the characteristic length of the geometry, L_c, which is taken here to be the step height H. ρ_u and ρ_b denote the density of unburned and burned mixtures, respectively. The impacts of T_{in}, X_{H_2} and ϕ are implicitly included by U_u, ρ_u and ρ_b.

Based on the hypothesis described in Section 4.2.1, we denote the common values of $\tilde{S}$ and $\tilde{\kappa}$ at the transition point by $\tilde{S}^*$ and $\tilde{\kappa}^*$. The pressure response curves shown in Fig. 13 indicate that there are three transition points among the four different operating regimes.

For fixed T_{in} and X_{H_2} (for a single curve in Fig. 13), we consider the high- and low-limit of ϕ in each operating regime as the critical equivalence ratios (ϕ^*) at which the transitions are observed. Thus, there are six ϕ^* for given T_{in} and X_{H_2}, as illustrated in Fig. 15: $\phi^* = \phi_1^-$, ϕ_1^+, ϕ_2^-, ϕ_2^+, ϕ_3^- and ϕ_3^+. The subscript number distinguishes the different transitions, whereas the superscript signs $-$ and $+$ denote high- and low-limit of ϕ, respectively, at which the combustor transitions from one regime to another.

For a given (T_{in}, X_{H_2}), we can identify unique values for ϕ^* using Fig. 13. Once all six different values of ϕ^* are identified for each (T_{in}, X_{H_2}) used in the experiment (total 9 combinations of T_{in} and X_{H_2}), we have a family of operating conditions at each transition point defined by ϕ^*, i.e., 9 cases of (T_{in}, X_{H_2}), which can be used to search for the values of $\tilde{S}^*$ and $\tilde{\kappa}^*$.

Table 3: A set of operating conditions corresponding to the high ϕ-limit of Mode I (ϕ_1^-).

Equivalence ratio, ϕ		**C_3H_8:H_2 (Volume ratio)**		
		100:0	**70:30**	**50:50**
T_{in} (K)	**300K**	0.65	0.62	0.55
	400K	0.57	0.53	0.49
	500K	0.52	0.48	0.41

In Table 3, for example, we show a set of operating conditions defined by (T_{in}, X_{H_2}) used in the experiment, along with the values of ϕ_1^- identified at each (T_{in}, X_{H_2}). The operating conditions listed in Table 3 all correspond to the high-limit of ϕ in Mode I. Therefore, according to our hypothesis described in Section 4.2.1, the common values of the characteristic stretch rate $\tilde{\kappa}$ and the characteristic flame speed $\tilde{S}$ should exist across these operating conditions. Given the operating conditions (T_{in}, X_{H_2}) along with the corresponding values of ϕ_1^-, the consumption speed is only a function of the flame stretch. Hence, at each condition, we vary the stretch rate κ and compute the consumption speed S_c using the strained flame code [12, 13]. The results are then normalized to obtain $\tilde{S}$ and $\tilde{\kappa}$, as defined in Eqs. (4) and (5). In Fig. 16(a), we plot $\tilde{S}$ as a function of $\tilde{\kappa}$, calculated at the operating conditions listed in Table 3. Each curve in the figure represents the relation between $\tilde{S}$ and $\tilde{\kappa}$ at a

given (T_{in}, X_{H_2}). We observe that the curves all intersect approximately at a single point; ($\tilde{S}$, $\tilde{\kappa}$) = (3.3×10^{-3}, 0.122), which essentially corresponds to ($\tilde{S}^*$, $\tilde{\kappa}^*$) for ϕ_1^-, supporting our hypothesis.

The same procedure is performed for all other transition points ϕ_1^+ and $\phi_i^\pm$ ($i = 2, 3$). Results are shown in Fig. 16(b-f), which are obtained using the operating conditions listed in Tables 5–9, respectively (see Appendix A). We observe that at each transition point, the $\tilde{S} - \tilde{\kappa}$ curves intersect nearly at a single point (with the exception of the cases, $T_{in} = 300$ K and $X_{H_2} = 50\%$; $T_{in} = 400$ K and $X_{H_2} = 30\%$), again confirming our hypothesis.

Table 4: The values of $\tilde{S}^*$ and $\tilde{\kappa}^*$ as identified by searching for the intersection points among the $\tilde{S} - \tilde{\kappa}$ curves in Fig. 16(a-f).

ϕ^*	$\tilde{S}^*$	$\tilde{\kappa}^*$
ϕ_1^-	3.3×10^{-3}	0.122
ϕ_1^+	3.7×10^{-3}	0.138
ϕ_2^-	5.2×10^{-3}	0.13
ϕ_2^+	5.7×10^{-3}	0.124
ϕ_3^-	6.6×10^{-3}	0.132
ϕ_3^+	7.1×10^{-3}	0.134

The intersection point ($\tilde{S}^*$, $\tilde{\kappa}^*$) for each ϕ^* is shown in Table 4. The value of $\tilde{S}^*$ monotonically increases as the combustor transitions from Mode I through Mode IIIb; this is expected since the value of ϕ^* increases from ϕ_1^- through ϕ_3^+. In contrast, the values of $\tilde{\kappa}^*$ across different transition points are approximately the same, suggesting the existence of a characteristic value of the stretch rate, denoted here by $\tilde{\kappa}_c^*$, across all the operating regimes of the combustor:

$$\tilde{\kappa}_c^* = \left(\frac{\rho_b}{\rho_u}\right) \frac{\bar{\kappa} H}{U_u} \approx 0.13 \tag{6}$$

Therefore, we calculate the values of the stretch rate over the range of conditions used in the experiments using Eq. (6) and plot them in Fig. 17:

$$\bar{\kappa}_c = 180 - 390 \text{ s}^{-1} \tag{7}$$

where $\bar{\kappa}_c$ increases with both equivalence ratio and inlet temperature, indicating that the flame is more stretched as the combustor becomes unstable. Figure 17 shows that the characteristic stretch rate is not significantly impacted by the mixture composition. The similar trends were shown by the stretch rate measurements presented in Section 4.1.3. Overall, the characteristic stretch rates shown in Fig. 17 show good agreement with the measurements shown in Table 2. The characteristic values (180−280 s^{-1} at T_{in} = 300 K) are slightly lower than the measured values (230−300 s^{-1}) but fall within the same range.

Indeed, the analysis presented in this section supports the hypothesis that a characteristic stretch rate $\tilde{\kappa}$ and a characteristic flame speed $\tilde{S}$ exist at the transition points where the combustor switches from one operating regime to another. It suggests, for example, that any two different mixtures exhibiting the same flame configuration near the transition point should share the same values of $\tilde{S}^*$ and $\tilde{\kappa}^*$ corresponding to that flame configuration. Moreover, we find a common value of the characteristic stretch rate for all the transition points, which are then used to estimate the stretch rate for the full range of operating conditions. In previous studies [10, 11], the value of stretch rate was chosen by trial and error until a value was found at which the pressure response curves collapse onto a single curve. The values suggested in this section are one order of magnitude lower than those used in [10], while being in the same range as the measured values presented in Section 4.1.

4.3. Collapse of experimental data

In this section, we verify the correlation of the characteristic stretch rate and flame speed with the experimental data. The strained flame consumption speed is computed at the characteristic stretch rate $\bar{\kappa}_c$ shown in Fig. 17 and the operating conditions used in the experiment. Figure 18 shows these values of S_c as a function of equivalence ratio for different inlet temperatures and fuel mixtures. The consumption speed varies within the range of 5−75 cm/s, where it increases with T_{in} or X_{H_2}. The impact of the operating parameters (T_{in}, X_{H_2} and ϕ) are indeed encapsulated in the consumption speed.

Now, we plot the pressure response curves shown in Fig. 13 against the non-dimensional flame speed parameter $\tilde{S}$ defined in Eq. (4). Since the values of $\tilde{S}$ are computed at the

characteristic stretch rate $\bar{\kappa}_c$, which is shared by all the operating conditions, we anticipate that $\tilde{S}$ collapses the data. Figure 19 shows that the data across all the inlet temperatures and fuel compositions nearly collapse onto a single curve, indicating that the dependence of the combustor response on the inlet temperature, fuel composition and equivalence ratio is converted into the dependence on the non-dimensional flame speed parameter alone. The transitions among distinct dynamic regimes occur approximately at $\tilde{S} \approx 0.0035$ (Mode I $\rightarrow$ Mode II), 0.005 (Mode II $\rightarrow$ Mode IIIa) and 0.0072 (Mode IIIa $\rightarrow$ Mode IIIb). Slight deviations are observed for some cases (e.g., $X_{H_2} = 30\%$ at $T_{in} = 400$ K and $X_{H_2} = 50\%$ at $T_{in} = 300$ K), which are expected from the scatter of the $\tilde{S} - \tilde{\kappa}$ curves for those cases, as shown in Fig. 16. Nevertheless, the results shown in Fig. 19 essentially support our hypothesis stated in Section 4.2.1. The various mixtures at different operating conditions share the same value of the characteristic flame speed at each transition point, where they experience the same "characteristic" flame stretch, exhibiting a similar flame configuration.

5. Conclusion

In this study, we examined the combustion dynamics driven by flame-vortex interactions in a laboratory scale backward-facing step combustor using the measurements of the dynamic pressure and the particle image velocimetry. The PIV data show distinct dynamics of the flame and flow among the different operating regimes, where the phase-averaged vorticity field and streamlines as well as the flame brush are generated to describe the interaction of the flame front with the flow structures. The flow properties, e.g., the flow fluctuations and accelerations as well as the size, location, circulation of the vortex structure, are quantified using the PIV data in each operating regime. The unstable operation (in Mode III) of the combustor is characterized by the kinematics of the large wake vortex, which drives the flame and flow fluctuations during the cycle. The vortex structure with large vorticity suddenly accelerates its convection downstream near the moment of the maximum flow fluctuation, while at the same moment, starting to rise toward the upper wall of the combustor. This motion, along with the flow reversal due to strong flow fluctuations, induces the flame flashback, which distinguishes Mode III from other operating regimes.

The PIV measurements are also used to quantify the stretch rate along the flame surface, which is induced by the interactions of the flow field (vortex structure) and the flame front. This work is intended to examine the values suggested in our previous study [10], which were found by trial and error for flame speed calculations with the aim of collapsing the pressure response data. The stretch rates estimated using the instantaneous flame front lines and the velocity field are one order of magnitude smaller than the values used in [10]. To systematically estimate the stretch rate for the full range of conditions used in the experiment, we use numerical results of the strained flame model [12, 13] along with the experimental data, and determine the characteristic stretch rate at the transition points identified by the dynamic pressure data. This analysis is based on the hypothesis that if distinct flames under different conditions exhibit a similar flame configuration, those flames should share common values of the "characteristic" stretch rate and flame speed, which induce that flame configuration. Indeed, we find common values of the normalized flame stretch and flame speed across a range of operating conditions (T_{in}, X_{H_2}) corresponding to each transition point. Moreover, a common value of the characteristic stretch rate across all the transition points is identified. The characteristic values also show good agreement with those measured using the PIV data. The non-dimensional flame speed parameter computed at the characteristic stretch rates successfully collapses the pressure response curves over the full range of conditions, demonstrating that the impact of different operating parameters are encapsulated in the characteristic flame speed alone. This result suggests that the stretch rate along the flame surface essentially captures the characteristics of the unsteady interaction between the flame front dynamics and the turbulent flow field, where the impact of the stretch rate is pronounced by its influence on the flame speed, which drives the flame propagation in the flow field. The fact that the dependence of distinct dynamics revealed by the PIV data on the operating conditions can be encapsulated in the consumption speed parameter suggests that local transport-chemistry interactions as well as turbulent flame propagation and kinematics represented by the flame speed plays an important role in determining overall system dynamics and their dependence on the various operating parameters.

The correlation developed in this study may be expanded for applications to other combustion systems of different geometry, operating at different conditions, although the form of non-dimensional parameter may vary, e.g., depending on the combustor geometry (and thus, flame anchoring configuration). We note that the non-dimensional flame speed and stretch rate parameters defined in Eqs. (4) and (5) incorporate the flow velocity as well as the characteristic geometric length, and thus, the impact of variations in those parameters should be reflected when correlating the combustor dynamics data. Similar analysis, for example, has been performed using the dynamics data obtained in a swirl-stabilized combustor [11, 48], burning syngas/air mixtures at Reynolds number of 25,000 (corresponding to an inlet velocity of 11.3 m/s at 300 K, which increases to 18.1 m/s at 400 K and 26.8 m/s at 500 K). The pressure response data were collapsed using the strained consumption speed [11] or using a non-dimensional flame speed parameter, similar to that defined in Eq. (4) [48].

If one considers gas turbine combustors that operate at higher pressure and temperature than those considered in this study, one should account for their impact on the structure and propagation of turbulent flames; e.g., burning rate, flame thickness, flame wrinkling (and hence, flame surface area) may change. As a result, the parametric space in which the combustor exhibits the instabilities can vary. In reality, the dependence of the flame shape (and dynamics) on the density ratio and the flame speed is certainly more complex than the form proposed here (e.g., Eq. 4), and those differences will be most pronounced across sudden changes in the flame shape, which define some of the observed mode-transitions. Nonetheless, the correlation presented here can be used as a framework for examining the combustor's stability characteristics, toward building the predictive capability for the onset of the dynamic instabilities in combustion systems.

Appendix A. Family of operating conditions with identical flame configuration

In Tables 5−9, we summarize the sets of operating conditions of high- and low-limits of ϕ in each operating regime, which can be identified using Fig. 13. As discussed in Section 4.2, the combustor exhibits nearly an identical flame configuration at the operating conditions in each set.

Table 5: The operating conditions corresponding to the low ϕ-limit of Mode II (ϕ_1^+)

Equivalence ratio, ϕ		**C_3H_8:H_2 (Volume ratio)**		
		100:0	**70:30**	**50:50**
T_{in} (K)	**300K**	0.67	0.63	0.56
	400K	0.59	0.54	0.50
	500K	0.53	0.49	0.42

Table 6: The operating conditions corresponding to the high ϕ-limit of Mode II (ϕ_2^-)

Equivalence ratio, ϕ		**C_3H_8:H_2 (Volume ratio)**		
		100:0	**70:30**	**50:50**
T_{in} (K)	**300K**	0.74	0.66	0.60
	400K	0.65	0.62	0.55
	500K	0.57	0.52	0.47

Table 7: The operating conditions corresponding to the low ϕ-limit of Mode IIIa (ϕ_2^+)

Equivalence ratio, ϕ		**C_3H_8:H_2 (Volume ratio)**		
		100:0	**70:30**	**50:50**
T_{in} (K)	**300K**	0.75	0.68	0.61
	400K	0.66	0.63	0.56
	500K	0.58	0.53	0.48

Table 8: The operating conditions corresponding to the high ϕ-limit of Mode IIIa (ϕ_3^-)

Equivalence ratio, ϕ		**C_3H_8:H_2 (Volume ratio)**		
		100:0	**70:30**	**50:50**
T_{in} (K)	**300K**	0.95	0.82	0.78
	400K	0.70	0.65	0.59
	500K	0.61	0.56	0.51

Table 9: The operating conditions corresponding to the low ϕ-limit of Mode IIIb (ϕ_3^+)

Equivalence ratio, ϕ		**C_3H_8:H_2 (Volume ratio)**		
		100:0	**70:30**	**50:50**
T_{in} (K)	**300K**	0.96	0.83	0.79
	400K	0.71	0.66	0.60
	500K	0.62	0.56	0.51

Acknowledgements

The authors would like to acknowledge the King Abdullah University of Science and Technology for their support of this research. This work was funded by the KAUST grant, number KUS-110-010-01.

References

[1] S. Ducruix, T. Schuller, D. Durox, S. Candel, Combustion dynamics and instabilities: elementary coupling and driving mechanisms, J. Propul. Power 19 (5) (2003) 722–734.

[2] K. K. Venkataraman, B. J. Lee, L. H. Preston, D. W. Simons, J. G. Lee, D. A. Santavicca, Mechanism of combustion instability in a lean premixed dump combustor, J. Propul. Power 15 (6) (1999) 909–918.

[3] D. Bernier, F. Lacas, S. Candel, Instability mechanisms in a premixed prevaporized combustor, J. Propul. Power 20 (4) (2004) 648–656.

[4] J. D. Sterling, E. E. Zukoski, Longitudinal Mode Combustion Instabilities in a Dump Combustor, 25th AIAA Aerospace Sciences Meeting (1987-0220).

[5] T. J. Poinsot, A. C. Trouve, D. P. Veynante, S. M. Candel, E. J. Esposito, Vortex driven acoustically coupled combustion instability, J. Fluid Mech. 177 (1987) 265–292.

[6] A. F. Ghoniem, S. Park, A. Wachsman, A. M. Annaswamy, D. Wee, H. Altay, Mechanism of combustion dynamics in a backward-facing step stabilized premixed flame, Proc. Combust. Inst. 30 (2005) 1783–1790.

[7] K. H. Yu, A. Trouve, J. W. Daily, Low-frequency pressure oscillations in a model ramjet combustor, J. Fluid Mech. 232 (1991) 47–72.

[8] K. I. Matveev, F. E. C. Culick, A model for combustion instability involving vortex shedding, Combust. Sci. Tech. 175 (2003) 1059–1083.

[9] K. Ahn, K. H. Yu, Effect of Damköhler number on vortex-flame interaction, Combust. Flame 159 (2012) 686–696.

[10] H. M. Altay, R. L. Speth, D. E. Hudgins, A. F. Ghoniem, Flame-vortex interaction driven combustion dynamics in a backward-facing step combustor, Combust. Flame 156 (2009) 1111–1125.

[11] R. L. Speth, A. F. Ghoniem, Using a strained flame model to collapse dynamic mode data in a swirl-stabilized syngas combustor, Proc. Combust. Inst. 32 (2009) 2993–3000.

[12] R. L. Speth, Y. M. Marzouk, A. F. Ghoniem, Impact of hydrogen addition on flame response to stretch and curvature, 43th AIAA Aerospace Sciences Meeting and Exhibit (2005-143).

[13] Y. M. Marzouk, A. F. Ghoniem, H. N. Najm, Toward a flame embedding model for turbulent combustion simulation, AIAA J. 41 (4) (2003) 641–652.

[14] M. Raffel, C. Willert, J. Kompenhans, Particle Image Velocimetry: a practical guide, Springer, Berlin, 1998.

[15] D. L. Reuss, R. J. Adrian, C. C. Landreth, Two-Dimensional Velocity Measurements in a Laminar Flame Using Particle Image Velocimetry, Comb. Sci. Tech. 67 (4-6) (1989) 73–83.

[16] J. F. Driscoll, D. J. Sutkus, W. L. Roberts, M. E. Post, L. P. Goss, The Strain Exerted by a Vortex on a Flame Determined from Velocity Field Images, AIAA 31st Aerospace Sciences Meeting and Exhibit (1993-0362).

[17] I. Boxx, C. Heeger, R. Gordon, B. Bohm, M. Aigner, A. Dreizler, W. Meier, Simultaneous three-component PIV/OH-PLIF measurements of a turbulent lifted C_3H_8-argon jet diffusion flame at 1.5kHz repetition rate, Proc. Combust. Inst. (2009) 905–912.

[18] I. Boxx, M. Stöhr, C. Carter, W. Meier, Temporally resolved planar measurements of transient phenomena in a partially premixed swirl flame in a gas turbine model combustor, Combust. Flame 157 (2010) 1510–1525.

[19] A. M. Steinberg, I. Boxx, M. Stöhr, C. D. Carter, W. Meier, Flow-flame interactions causing acoustically coupled heat release fluctuations in a thermo-acoustically unstable gas turbine model combustor, Combust. Flame 157 (2010) 2250–2266.

[20] A. M. Steinberg, J. F. Driscoll, S. L. Ceccio, Measurements of turbulent premixed flame dynamics using cinema stereoscopic PIV, Exp. Fluids 44 (2008) 985–999.

[21] A. M. Steinberg, J. F. Driscoll, S. L. Ceccio, Temporal evolution of flame stretch due to turbulence and the hydrodynamic instability, Proc. Combust. Inst. 32 (2009) 1713–1721.

[22] A. M. Steinberg, J. F. Driscoll, Straining and wrinkling process during turbulence-premixed flame interaction measured using temporally resolved diagnostics, Combust. Flame 156 (2009) 2285–2306.

[23] A. M. Steinberg, J. F. Driscoll, Stretch-rate relationships for turbulent premixed combustion LES subgrid models measured using temporally resolved diagnostics, Combust. Flame 157 (2010) 1422–1435.

[24] S. A. Filatyev, J. F. Driscoll, C. D. Carter, J. M. Donbar, Measured properties of turbulent premixed flames for model assessment, including burning velocities, stretch rates, and surface densities, Combust. Flame 141 (2005) 1–21.

[25] D. Englund, W. B. Richards, The infinite line pressure probe, Technical Report NASA TM-83582, National Aeronautics and Space Administration, 1984.

[26] R. L. Speth, H. M. Altay, D. E. Hudgins, A. F. Ghoniem, Dynamics and stability limits of syngas combustion in a backward-facing step combustor, Proceedings of ASME Turbo Expo (GT2007-28130).

[27] R. L. Speth, S. Hong, S. J. Shanbhogue, A. F. Ghoniem, Mode selection in flame-vortex driven combustion instabilities, 49th AIAA Aerospace Sciences Meeting (2011-236).

[28] R. L. Speth, H. M. Altay, D. E. Hudgins, A. F. Ghoniem, Dynamics and stability limits of syngas combustion in a swirl-stabilized combustor, Proceedings of ASME Turbo Expo (GT2008-51023).

[29] S. Hong, R. L. Speth, S. J. Shanbhogue, A. F. Ghoniem, Mode transitions in flame-vortex driven combustion instabilities, in preparation .

[30] A. K. M. F. Hussain, Coherent structures and turbulence, J. Fluid Mech. 173 (1986) 303–356.

[31] L. Lourenco, S. Subramanian, Z. Ding, Time series velocity field reconstruction from PIV data, Meas. Sci. Technol. 8 (1997) 1533–1538.

[32] J. Sung, J. Y. Yoo, Three-dimensional phase averaging of time-resolved PIV measurement data, Meas. Sci. Technol. 12 (2001) 655–662.

[33] S. A. Filatyev, M. P. Thariyan, R. P. Lucht, J. P. Gore, Simultaneous stereo particle image velocimetry and double-pulsed planar laser-induced fluorescence of turbulent premixed flames, Combust. Flame 150 (2007) 201–209.

[34] S. Pfadler, A. Leipertz, F. Dinkelacker, Systematic experiments on turbulent premixed Bunsen flames including turbulent flux measurements, Combust. Flame 152 (2008) 616–631.

[35] Q. Zhang, S. J. Shanbhogue, Shreekrishna, T. Lieuwen, J. O'Connor, Strain Characteristics Near the Flame Attachment Point in a Swirling Flow, Combust. Sci. Tech. 183 (7) (2011) 665–685.

[36] N. Peters, Turbulent Combustion, Cambridge University Press, 2000.

[37] C. Meneveau, T. Poinsot, Stretching and Quenching of Flamelets in Premixed Turbulent Combustion, Combust. Flame 86 (1991) 311–332.

[38] S. Pfadler, F. Beyrau, A. Leipertz, Flame front detection and characterization using conditioned particle image velocimetry, Optics Express 15 (2007) 15444–15456.

[39] J. Canny, A computational approach to edge detection, IEEE Transactions on Pattern Analysis and Machine Intelligence PAMI-8 (6) (1986) 679–698.

[40] S. M. Candel, T. J. Poinsot, Flame stretch and the balance equation for the flame area, Combust. Sci. and Tech. 70 (1990) 1–15.

[41] C. K. Law, Combustion Physics, Cambridge University Press, Cambridge, 2006.

[42] J. F. Driscoll, Turbulent premixed combustion − flamelet structure and turbulent burning velocities, Prog. Energy Combust. Sci. 34 (2008) 91–134.

[43] P. Lavoie, G. Avallone, F. D. Gregorio, G. P. Romano, R. A. Antonia, Spatial resolution of PIV for the measurement of turbulence, Exp. Fluids 43 (2007) 39–51.

[44] N. Peters, Laminar flamelet concepts in turbulent combustion, Proceedings of the Twenty-First International Symposium on Combustion (1986) 1231–1250.

[45] N. Peters, The turbulent burning velocity for large scale and small scale turbulence, J. Fluid Mech. 384 (1999) 107–132.

[46] D. Goodwin, Cantera: Object-oriented software for reacting flows, 2005.

[47] M. V. Petrova, F. A. Williams, A small detailed chemical-kinetic mechanism for hydrocarbon combustion, Combust. Flame 144 (2006) 526–544.

[48] R. L. Speth, Fundamental Studies in Hydrogen-Rich Combustion: Instability Mechanisms and Dynamic Mode Selection, Ph.D. thesis, Massachusetts Institute of Technology, 2010.

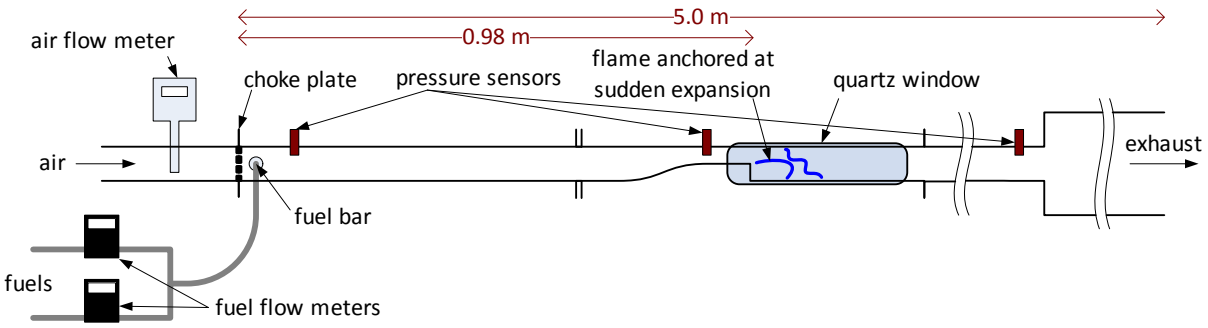

Figure 1: Schematic of the backward-facing step combustor with instrumentation

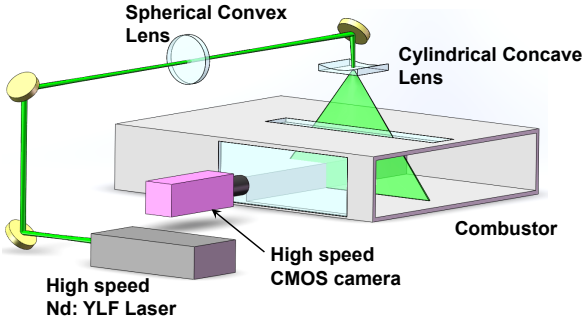

Figure 2: Apparatus for high-speed particle image velocimetry in the backward-facing step combustor

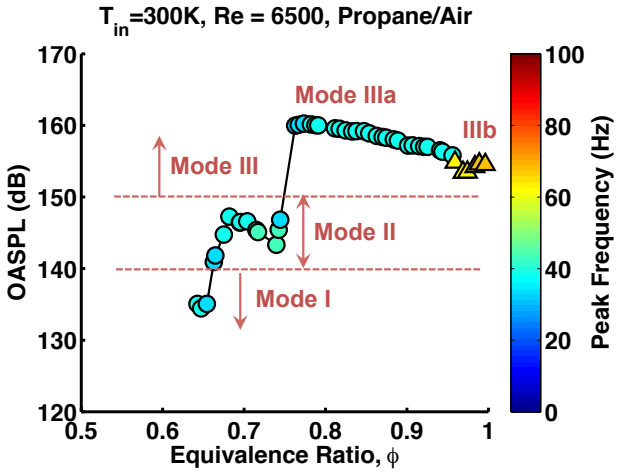

Figure 3: The overall sound pressure level (OASPL) as a function of the equivalence ratio for a propane/air mixture at T_{in} = 300 K and Re = 6500. The pressure is measured at 0.2 m upstream of the sudden expansion. The peak frequency at each equivalence ratio is represented by a color shown in the side bar. The typical operating regimes are designated as Mode I, Mode II, Mode IIIa (○) and Mode IIIb (△).

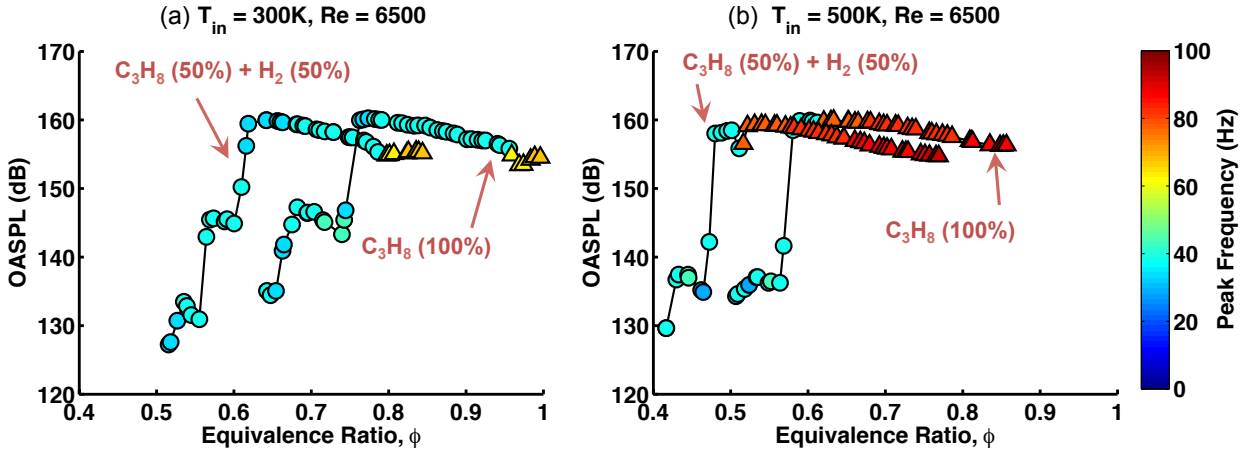

Figure 4: The pressure response curves (OASPL as a function of ϕ) for (a) T_{in} = 300 K and (b) T_{in} = 500 K. At each inlet temperature, the cases with different mixture composition (volume ratio) are shown: propane/air flame and propane(50%)/hydrogen(50%)/air flame. Re = 6500 for all cases.

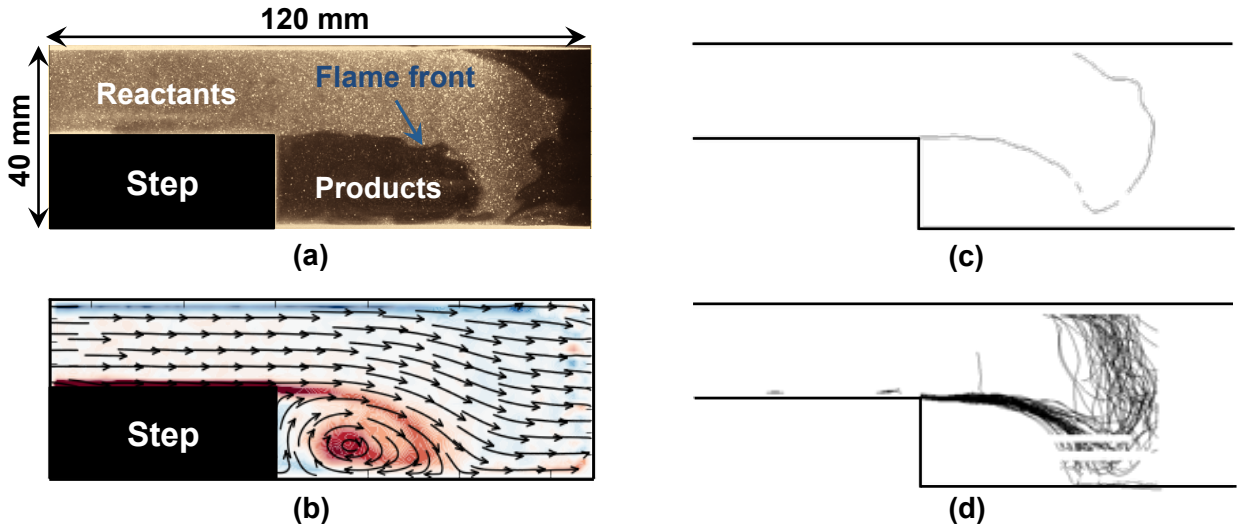

Figure 5: The sample images of the high speed PIV data: (a) a raw seeding particle image; (b) the phase-averaged vorticity field (colored region; red in clockwise direction and blue in counter clockwise direction) and the streamlines (black arrows); (c) an instantaneous flame front line detected from a seeding particle image; (d) the flame brush−instantaneous flame lines overlapped at a given phase during the cycle; (b)−(d) are used to examine the flame-flow interaction in each operating regime.

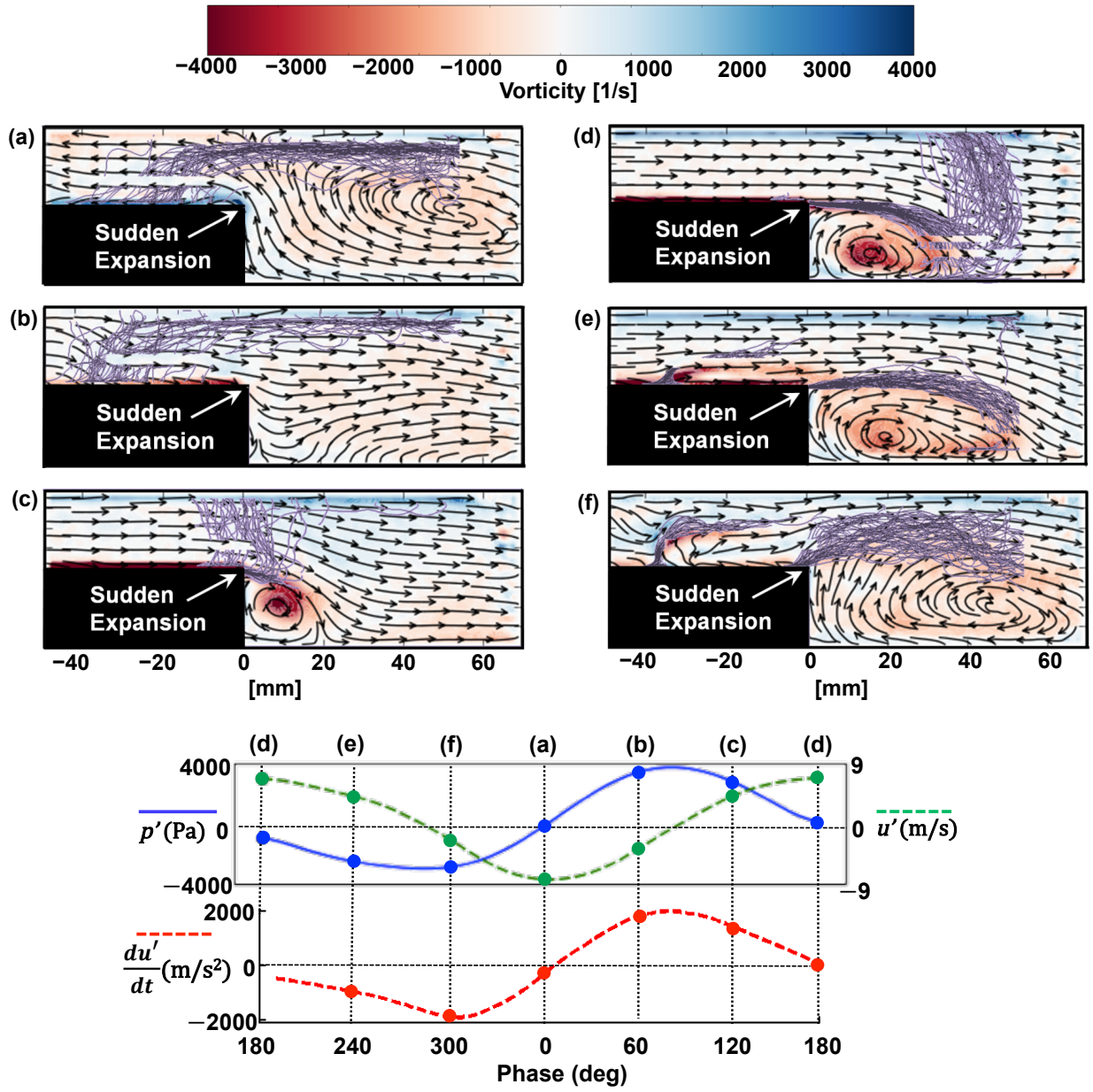

Figure 6: The vorticity (colored regions: red in clockwise direction and blue in counter clockwise direction), streamlines (black arrows) and flame brush (lavender lines) for Mode IIIa, shown at six different phases of the instability cycle. The plot at the very bottom shows pressure and velocity fluctuations measured upstream of the sudden expansion as well as the flow acceleration, as a function of the phase during the cycle. The instability period is $\sim$ 0.025 s (40 Hz). Conditions: C_3H_8/Air, $\phi = 0.75$, $T_{in} = 300$ K and Re = 6500. Mean inlet velocity is $\sim$5 m/s.

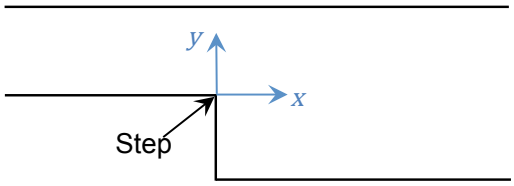

Figure 7: An illustration showing the x- and y-coordinates used in Figs. 8 and 10.

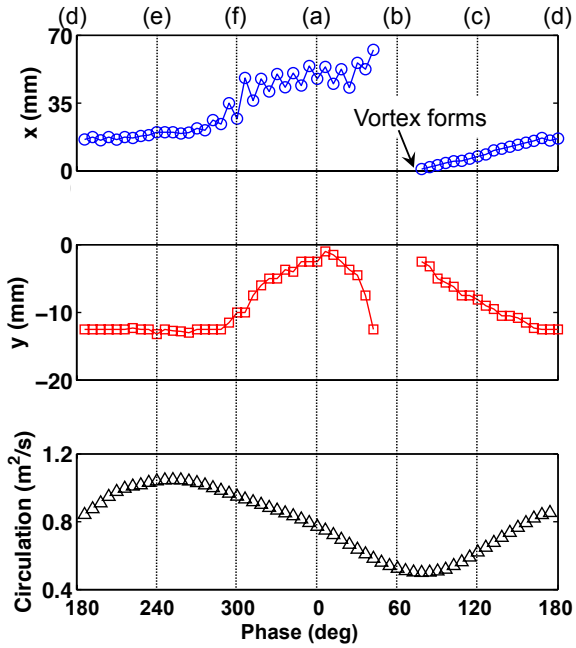

Figure 8: The x- (top) and y-position (middle) of the vortex core, i.e., distance from the vertical and horizontal edge of the step, as a function of the phase in Mode IIIa. The bottom plot shows the total circulation of the vortex, i.e., the vorticity integrated over the vortex structure during the cycle.

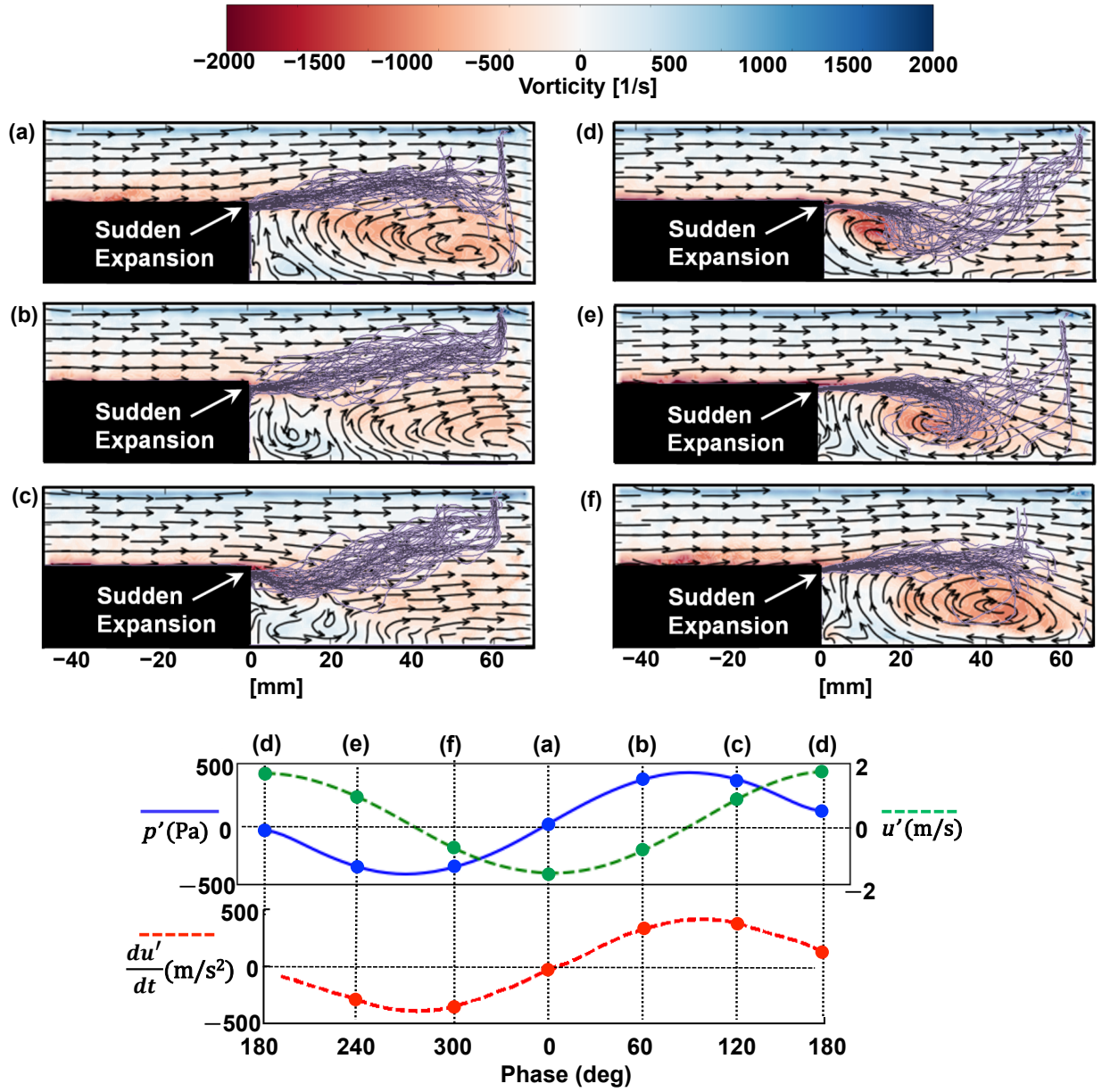

Figure 9: The vorticity (colored regions: red in clockwise direction and blue in counter clockwise direction), streamlines (black arrows) and flame brush (lavender lines) for Mode II (oscillating at 40 Hz), shown at six different phases of the instability cycle. The plot at the very bottom shows pressure and velocity fluctuations measured upstream of the sudden expansion as well as the flow acceleration, as a function of the phase during the cycle. Conditions: $C_3H_8(50\%)/H_2(50\%)/\text{Air}$, $\phi = 0.58$, $T_{in} = 300$ K and Re = 6500. Mean inlet velocity is $\sim$5 m/s.

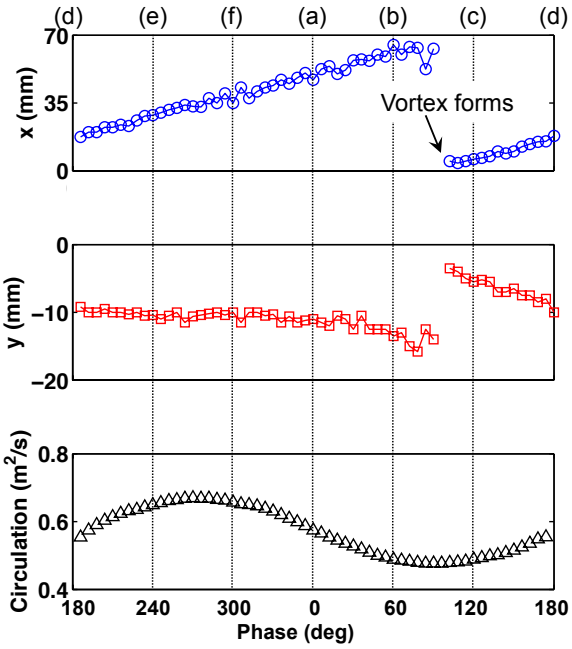

Figure 10: The x- (top) and y-position (middle) of the vortex center, i.e., distance from the vertical and horizontal edge of the step, as a function of the phase in Mode II. The bottom plot shows the total circulation of the vortex, i.e., the vorticity integrated over the vortex structure during the cycle.

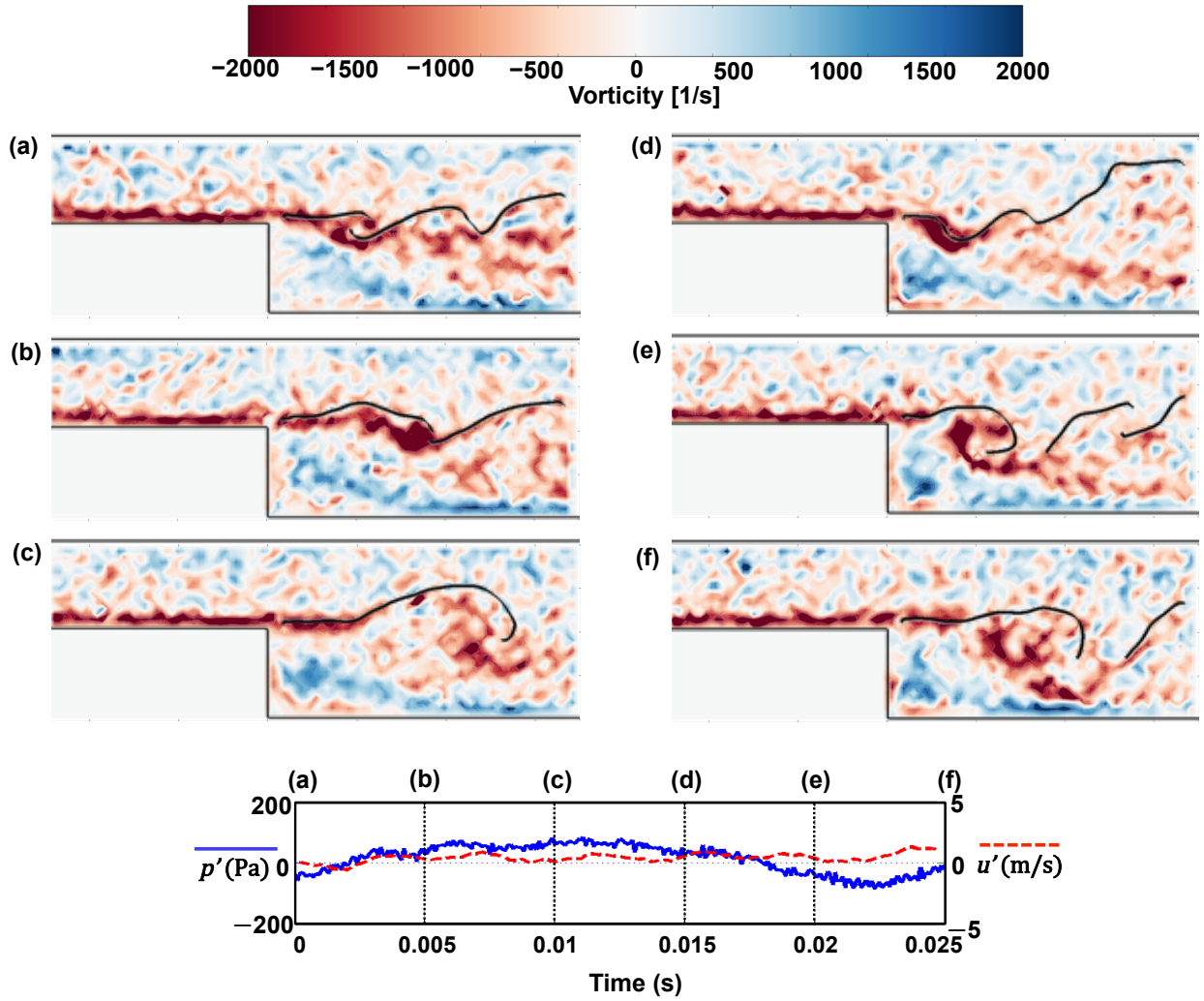

Figure 11: Instantaneous images of the vorticity (colored regions: red in clockwise direction and blue in counter clockwise direction) and the flame front position (black lines) for Mode I, shown for the same time period as one cycle of 40 Hz instability. Conditions: $C_3H_8(70\%)/H_2(30\%)$/Air, $\phi = 0.62$, $T_{in} = 300$ K, Re = 6500.

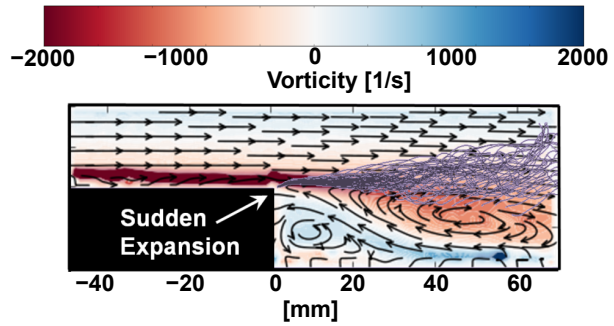

Figure 12: The time-average vorticity (colored regions: red in clockwise direction and blue in counter clockwise direction), streamlines (black arrows) and flame brush (lavender lines) for Mode I. Total $\sim$ 1000 images are averaged. Conditions: $C_3H_8(70\%)/H_2(30\%)$/Air, ϕ = 0.62, T_{in} = 300 K, Re = 6500.

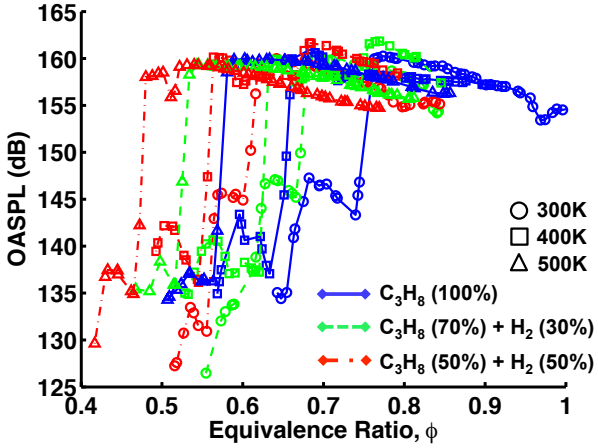

Figure 13: The overall sound pressure level (OASPL) as a function of equivalence ratio over a range of fuel compositions and inlet temperatures. The response curves shift to the left as either the inlet temperature or hydrogen concentration in fuel mixture increases. Re = 6500 for all cases.

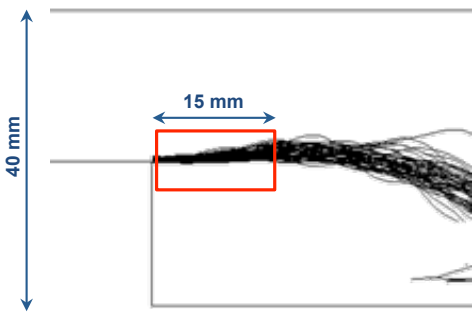

Figure 14: A sample image showing the ensemble of the instantaneous flame front lines, where the red box is the region in which the stretch rates are computed along each flame front line. The measurements are obtained with the grid size of 0.143 mm and the vector spacing of 1.14 mm. The detailed properties of the PIV measurement are described in Table 1.

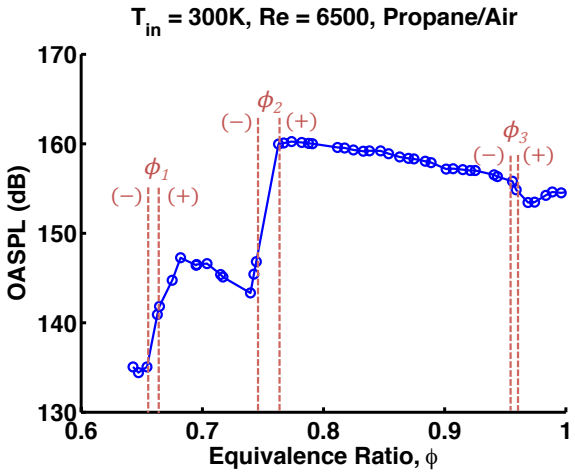

Figure 15: The pressure response curve showing the critical equivalence ratios, ϕ^* at the transitions between distinct operating regimes. The high- and low-limit of ϕ in each regime are denoted by $(-)$ and $(+)$, respectively.

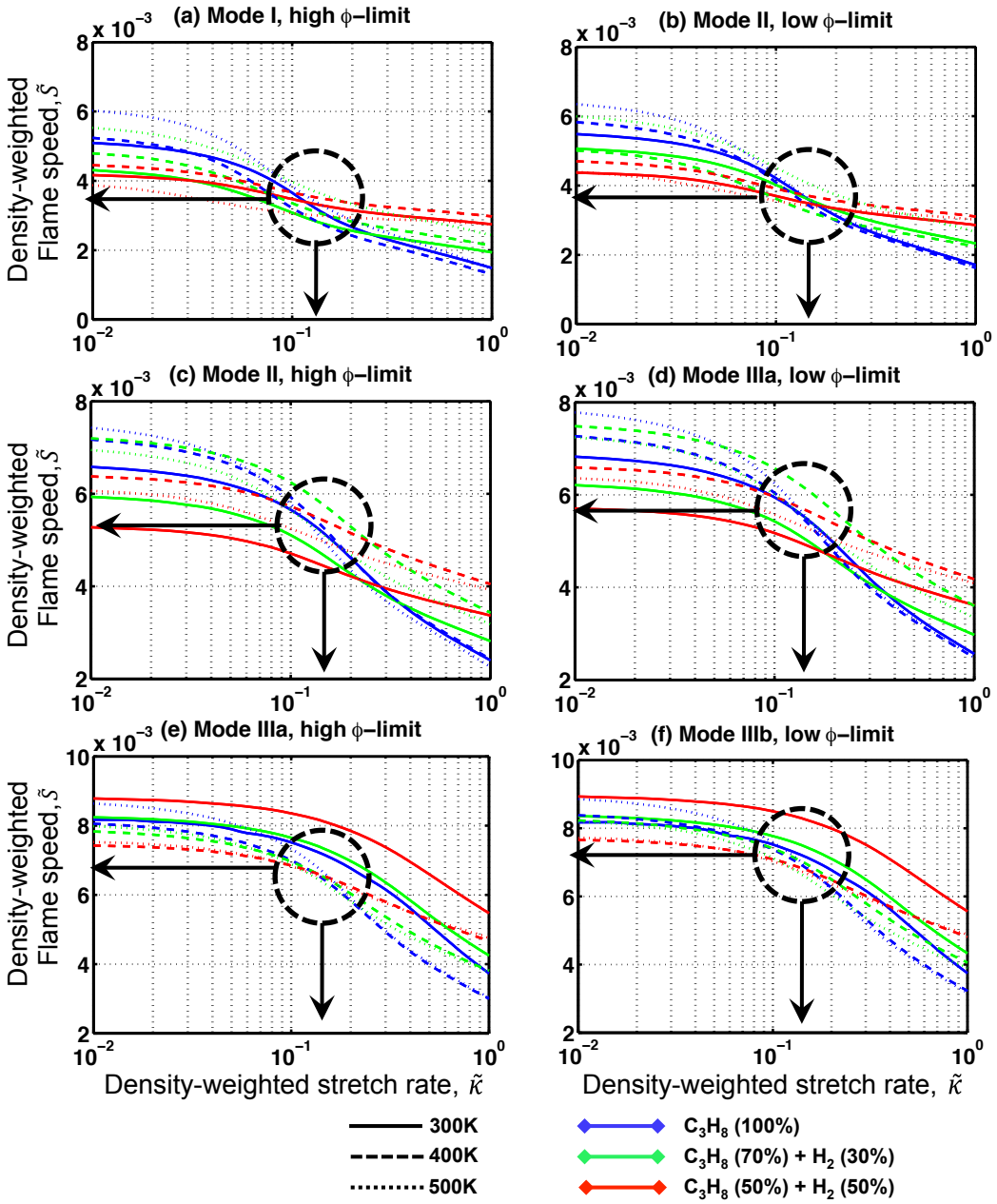

Figure 16: Density-weighted flame speed $\tilde{S}$ as a function of density-weighted stretch rate $\tilde{\kappa}$ at the operating conditions shown in Tables 3 and 5−9, at which dynamic mode transitions are observed. Each sub-figure represents a transition point at which the combustor switches from one operating regime to another. $\tilde{S}$ and $\tilde{\kappa}$, which are dimensionless, are defined in Eqs. (4) and (5), respectively. The dependence of the flame consumption speed on the stretch rate was computed using the strained flame code [12, 13], and the data are normalized and plotted. The circle and arrows in each sub-figure show that $\tilde{S}-\tilde{\kappa}$ curves obtained at different conditions (T_{in} and X_{H_2}) approximately intersects at a single point, having common values of $\tilde{S}$ and $\tilde{\kappa}$ as summarized in Table 4.

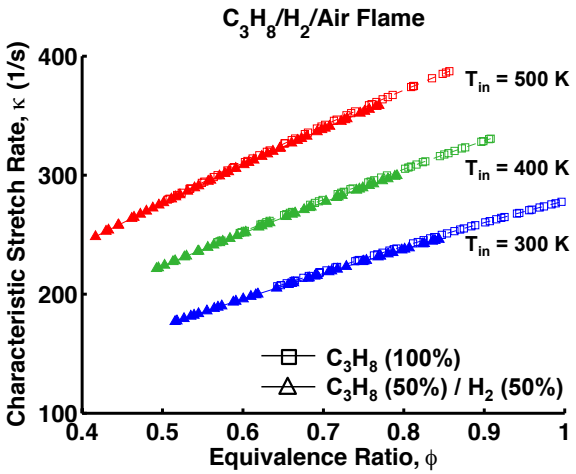

Figure 17: The value of characteristic stretch rate κ_c indicated by Eq. (6) depending on the operating conditions.

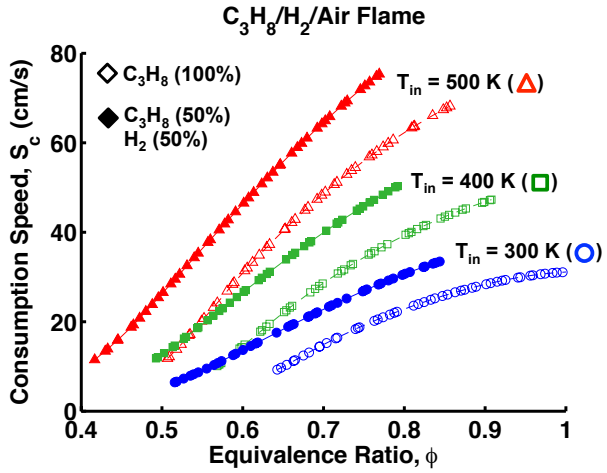

Figure 18: Variation in the consumption speed computed at the characteristic stretch rate and the conditions used in the experiment. Open symbols indicate $C_3H_8(100\%)$ and closed symbols indicate $C_3H_8(50\%)/H_2(50\%)$: ○ T_{in} = 300 K; □ T_{in} = 400 K; △ T_{in} = 500 K.

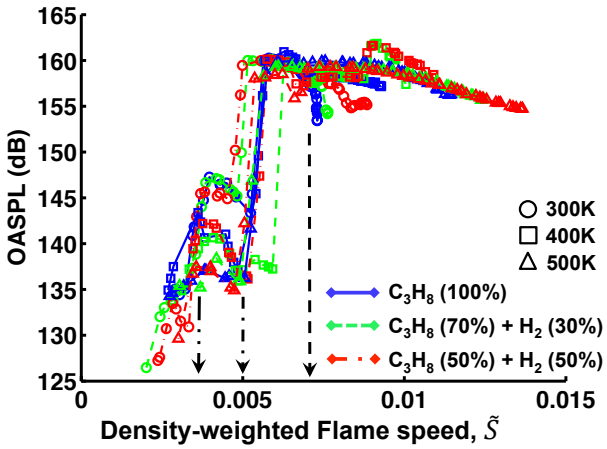

Figure 19: The overall sound pressure level (OASPL) as a function of density-weighted flame speed $\tilde{S}$. The curves shown in Fig. 13 approximately collapse onto a single curve, demonstrating that the dependence of dynamic regimes on the inlet temperature, fuel composition and equivalence ratio is encapsulated in $\tilde{S}$ alone.